The Formation of Seaward-dipping Reflectors in Volcanic Margins: Insights from High-resolution Visco-elasto-plastic Geodynamic Models with Extrusive Surface Processes

Erik Arthur Kneller

eknellerr@geonomylabs.com

Geonomy Labs
2002 Timberloch Place
The Woodlands, TX 77380
USA

Peer-review status: This manuscript is a non-peer-reviewed preprint of a research article that has been submitted to *Physics of the Earth and Planetary Interiors*.

November 28, 2025

The Formation of Seaward-dipping Reflectors in Volcanic Margins: Insights from High-resolution Visco-elasto-plastic Geodynamic Models with Extrusive Surface Processes

Erik Arthur Kneller

Geonomy Labs, 2002 Timberloch Place, The Woodlands, TX, 77380, USA

Abstract

Seismic reflection data from volcanic margins show thick packages of seaward-dipping reflectors (SDRs) that are commonly interpreted as buried subaerial lava flows. The origins of SDRs remain debated with proposed mechanisms including (1) syn-kinematic extrusion of lava flows on extended continental crust, (2) progressive rotation of subaerial lava flows due to volcanic loading and magmatic spreading and (3) syn-kinematic emplacement of lava flows on mobile gabbroic basement. This study presents the first systematic investigation of SDR formation using high-resolution visco-elasto-plastic geodynamic models with melt processes coupled to a surface processes model that includes sediment transport and extrusive lava-flow emplacement based on a cellular automata approach. These numerical experiments demonstrate that the typical frictional-plastic strain-weakening model commonly used in geodynamic models does not generate the symmetric, seaward-dipping lava flows and low-relief gabbroic basement structures interpreted from seismic reflection data. Instead, these models generate large off-axis extensional faults in thick volcanic packages and create large graben where thick syn-kinematic lava flows accumulate, driving ductile deformation and the formation of high-relief ($>$ 2 km) ridges in the underlying hot, accreting gabbroic crust. The models presented in this work also demonstrate that reproducing observed seaward-dipping lava-flow geometries and low-relief gabbroic basement structures requires an additional melt-damage weakening mechanism above zones of melt focusing that approximates the effects of channelized melt networks and dike injection on lithospheric rheology. This melt-damage model probabilistically reduces friction coefficients and cohesion in the melt-extraction zone and produces seaward-dipping geometries by stabilizing the spreading axis and promoting more widely distributed subaerial flows that undergo rotation due to spreading-induced separation and burial by younger lava-flow packages. Finally, it is shown that the detailed geometry of lava-flow packages is controlled by the duration of the inter-eruption period with longer inter-eruption periods leading to a larger eruption volume that fills in axial depressions, builds up relatively flat axial plateaus, and produces more

symmetric seaward-dipping geometries with smoother upward convexity.

Contents

1 Introduction **3**

2 Methods **4**
2.1 Governing Equations 5
2.1.1 Conservation of Momentum and Mass 5
2.1.2 Conservation of Energy 7
2.2 Topography Advection, Sediment Transport and Compaction . . 9
2.3 Melt Generation, Transport and Emplacement 12
2.4 Melt Extrusion and Lava Flow 17
2.5 Composite Viscous Creep 20
2.6 Strain Weakening and Melt Damage 22

3 Model Setup **25**

4 Results **26**
4.1 Base Case: Magmatic Crust Formation with Melt Damage 27
4.2 The Critical Role of Probabilistic Melt Damage 27
4.3 Effect of Maximum Melt Damage Factor 27
4.4 Effect of Melt Damage Zone Width 28
4.5 Effect of Inter-Eruption Period 28
4.6 Effect of Maximum Extrusion Factor 28
4.7 Effect of Thermal Anomaly 29
4.8 Effect of Characteristic Subaerial Flow Length 29

5 Discussion and Conclusions **29**

Tables **33**

Figures **41**

Appendix **53**

Appendix A Algorithm for Solving the Visco-elasto-plastic Stokes-Continuity Equations **53**
Appendix A.0.1 Picard Iteration Loop 54
Appendix A.0.2 Nodal Plasticity Update 56
Appendix A.0.3 Harmonic Viscosity Average for Yielding . . . 57
Appendix A.0.4 Subgrid Stress Diffusion Steps 58

Email address: eknellerGgeonomylabs.com (Erik Arthur Kneller)

Appendix B Algorithm for Solving the Heat Advection-Diffusion Equation **59**
Appendix B.0.1 Subgrid Thermal Diffusion Steps 59

Appendix C Marker-grid Interpolation **60**

Appendix D Non-Linear Creep Viscosity Update Steps **62**

References **64**

1. Introduction

Seismic reflection data from extensional margins in the North Atlantic, Central Atlantic, South Atlantic, Gulf of Mexico, and Western India often reveal thick packages of high-amplitude dipping reflectors that diverge and increase in dip toward the ocean [1, 2, 3, 4, 5, 6]. These seaward-dipping reflectors (SDRs) are commonly interpreted as buried subaerial lava flows [2, 3, 4, 5, 6]. Reconstructions of SDR packages across conjugate margins suggest that SDRs formed in a symmetric manner around a spreading center [4]. The observation of widespread SDRs and measured crustal seismic velocities consistent with thick mafic material have been used to classify many margins with SDRs as volcanic passive margins where relatively thin crust may be composed entirely of new magmatic and volcanic material as opposed to extended pre-existing continental crust [1, 7, 5].

SDR packages have been classified by [4] into two main categories. The first is Type I SDRs that are associated with tectonically controlled proximal fault-bound wedges with planar geometries that downlap onto inclined basement with fault-controlled relief. Type I SDRs have reflector lengths ranging from 1-51 km, total lava flow thickness less than 10 km and dips ranging from 2 to 28° with a mean dip of 14° [4]. The second is Type II SDRs that form on actively spreading magmatic crust with diverging packages of reflectors that increase in upward convexity in the down dip direction and downlap onto sub-horizontal opaque basement with low relief. Type II SDRs have reflector lengths ranging from 1-91 km, total thickness less than 15 km, and dips ranging from 0 to 30° with a mean dip of 8° [4]. Type II SDRs generally increase in dip in the down dip direction and have been observed to display downward convexity close to where reflectors downlap onto sub-horizontal basement [4].

Despite their widespread nature, the origins of SDRs and associated basement structures remain debated with proposed mechanisms including (1) syn-kinematic extrusion of lava flows on extended continental crust [1], (2) progressive rotation of subaerial lava flows due to volcanic loading and spreading of magmatic crust [3], and (3) syn-kinematic emplacement of lava flows on mobile gabbroic basement [2, 8]. Assessing the plausibility of these mechanisms has implication for paleogeographic reconstructions and models of thermal evolution of the lithosphere and asthenosphere. Geodynamic models that couple mantle melting with lava flow emplacement can be used to test the plausibility of these

mechanisms by constraining processes and structural evolution with conservation laws that use boundary and initial conditions consistent with geologic and geophysical observations.

Recent geodynamic modeling studies have made progress on producing a level of geologic realism that is required to adequately compare forward modeling results to observations from extensional margins by (1) applying higher numerical resolution required to resolve shear zones [9, 10], (2) introducing polyphase boundary conditions consistent with plate reconstructions [9], (3) coupling lithospheric deformation with erosion and sediment transport [11, 12], (4) using isostatically consistent sea level [13], and (5) including melting processes [14, 15, 16, 17]. Modeling magmatic crust formation and lava flow emplacement requires building on this recent work and introducing new methods for coupling long-term geodynamic deformation processes that occur over millions of years with extrusive surface processes that occur over days to tens of thousands of years.

Previous models of SDR formation have either been conceptual [4] or based on numerical calculations that use a half-spreading-center modeling approach that lacks full lithospheric extension, realistic visco-elasto-plastic rheology, coupling between deformation and magmatic processes and lava flow emplacement [18, 19]. Here, the formation of dipping subaerial lava flows and magmatic crust is investigated using high-resolution visco-elasto-plastic marker-in-cell geodynamic models with melt generation, instantaneous melt transport and emplacement, and a surface processes model that includes erosion and sediment transport and a new extrusive lava flow model based on a cellular automata approach (Figure 5). This melt extrusion model takes into account subaerial vs submarine flow conditions, the availability of magma for extrusion, and the inter-eruption period associated with large subaerial volcanic eruptions. An additional focus of this study is how lithospheric rheological parameters control the geometry of buried lava flow packages. A probabilistic frictional-plastic melt-damage weakening model is introduced that approximates the effects of channelized melt networks and dike injection on lithospheric strength above regions of melt focusing in the partially molten mantle (Figure 5). This melt-damage weakening model is spatially and temporally coupled to active melting processes and plays an important role in controlling the evolution and geometry of buried lava-flow packages and magmatic crust structure.

2. Methods

The numerical models presented in this work were implemented using EarthBox.jl, a Julia package for multiphase visco-elasto-plastic marker-in-cell geodynamic modeling with melt generation, melt intrusion, melt extrusion, frictional-plastic melt damage, lava flow modeling and marine and terrestrial sediment transport with compaction [20]. EarthBox.jl discretizes the Stokes-continuity and heat transport equations on a staggered grid using conservative finite differences and free-surface stabilization [21, 22]. Advective processes are modeled

using a 4-th order Runge-Kutta scheme that includes both grid and subgrid changes in temperature and deviatoric stress [21].

The fundamental aspects of the marker-in-cell approach for solving incompressible flows with a free-surface used by EarthBox.jl were first published by [23]. This approach was later modified for visco-elasto-plastic problems by [24, 25, 21]. EarthBox.jl uses a visco-elasto-plastic thermo-mechanical algorithm that closely follows the algorithm described by [21] but with a node-based plasticity approach from [22] to improve the convergence of the non-linear visco-elasto-plastic Stokes-continuity solver Appendix A.

The following sections provide a detailed description of methods required to generate the numerical models presented in this work including specific formulations of the governing equations, sediment transport modeling with compaction, melt generation, extraction and transport, lava flow modeling and rheological models for viscous creep and frictional-plastic failure. The reader is referred to the EarthBox.jl documentation for additional details [20].

2.1. Governing Equations

2.1.1. Conservation of Momentum and Mass

Velocity and pressure are obtained by solving the conservation of momentum and mass equations for a slow, highly viscous incompressible visco-elasto-plastic fluid:

$$\frac{\partial \sigma'_{xx}}{\partial x} + \frac{\partial \sigma'_{xy}}{\partial y} - \frac{\partial P}{\partial x} = -\rho g_x \tag{1}$$

$$-\frac{\partial \sigma'_{xx}}{\partial y} + \frac{\partial \sigma'_{xy}}{\partial x} - \frac{\partial P}{\partial y} = -\rho g_y \tag{2}$$

$$f_{ve} = \frac{\eta_{vp}}{\mu \Delta t + \eta_{vp}} \tag{3}$$

$$\sigma'_{xx} = 2\eta_{vp}\dot{\epsilon}'_{xx}(1 - f_{ve}) + \sigma'^{co}_{xx} f_{ve} \tag{4}$$

$$\sigma'_{xy} = 2\eta_{vp}\dot{\epsilon}_{xy}(1 - f_{ve}) + \sigma'^{co}_{xy} f_{ve} \tag{5}$$

$$\dot{\epsilon}_{xx} = \frac{\partial v_x}{\partial x}, \quad \dot{\epsilon}_{xy} = \frac{1}{2}\left(\frac{\partial v_x}{\partial y} + \frac{\partial v_y}{\partial x}\right) \tag{6}$$

$$\frac{\partial v_x}{\partial x} + \frac{\partial v_y}{\partial y} = 0 \tag{7}$$

where σ'_{xx} is the deviatoric normal stress, σ'^{co}_{xx} is the corrected deviatoric normal stress from the previous time step, σ'_{xy} is the deviatoric shear stress, σ'^{co}_{xy} is the corrected deviatoric shear stress from the previous time step, P is the pressure, ρ is the density, g_x and g_y are the gravitational accelerations, η_{vp} is the visco-plastic viscosity, μ is the shear modulus, Δt is the computational time step,

$\dot{\epsilon}'_{xx}$ is normal deviatoric strain rate, $\dot{\epsilon}'_{xy}$ is the deviatoric shear strain rate and v_x and v_y are the velocity components. Equations (1) and (2) are the x- and y-components of the Stokes equations, respectively. It is noted that equation (2) utilizes the relationships $\sigma'_{yy} = -\sigma'_{xx}$ and $\sigma'_{yx} = \sigma'_{xy}$ to reduce computational storage requirements. The Boussinesq approximation is used to account for the effects of temperature and pressure on density in the gravitation terms in (1) and (2) while maintaining the assumption of incompressibility from (7):

$$\rho = \rho_{ref}\left(1 - \alpha(T - T_{ref})\right)\left(1 + \beta(P - P_{ref})\right) \tag{8}$$

where ρ_{ref} is the reference density, α is the thermal expansion coefficient, T_{ref} is the reference temperature (298.15 K), β is the compressibility coefficient, and P_{ref} is the reference pressure (10^5 Pa). Gravitational acceleration in the x-direction (g_x) is set equal to zero, and gravitational acceleration in the y-direction (g_y) is set equal to 9.8 m/s^2. The visco-plastic viscosity term η_{vp} is given by:

$$\begin{aligned} \eta_{vp} &= \eta_{creep} \quad \text{for} \quad \sigma_{II,elastic} \leq \sigma_{yield}, \text{ and} \\ \eta_{vp} &= \mu\Delta t \frac{\sigma_{yield}}{\sigma_{II,elastic} - \sigma_{yield}} \quad \text{for} \quad \sigma_{II,elastic} > \sigma_{yield} \end{aligned} \tag{9}$$

where η_{creep} is the viscosity associated with creep mechanisms, σ_{yield} is the yield stress and $\sigma_{II,elastic}$ is the second invariant for purely elastic stress buildup [22] as given by

$$\sigma_{II,elastic} = \frac{\mu\Delta t + \eta_{creep}}{\eta_{creep}}\sigma_{II} \tag{10}$$

where σ_{II} is the second invariant of the stress tensor given by

$$\sigma_{II} = \sqrt{\left(\sigma_{xy}^2 + \sigma_{xx}^2\right)}. \tag{11}$$

Visco-plastic viscosity η_{vp} is limited by a minimum value of 10^{18} Pa·s and a maximum value of 10^{26} Pa·s. The yield stress σ_{yield} is given by the following equations:

$$\sigma_{yield} = \begin{cases} \sigma_c \cos\theta + \sin\theta\,(P - P_f) & \text{for} P \geq P_f \\ \sigma_c \cos(\theta) & \text{for} P < P_f \end{cases} \tag{12}$$

where σ_c is the cohesion, θ is the friction angle, and P_f is the fluid pressure. Yield stress is limited by a minimum value of 1 MPa.

The corrected deviatoric stresses from previous time steps, σ'^{co}_{xx} and σ'^{co}_{xy}, which appear in equations (4) and (5), take into account rotation using the following equations:

$$\sigma'^{co}_{xx} = \sigma'_{xx}\left(\cos(\omega\Delta t)^2 - \sin(\omega\Delta t)^2\right) - \sigma'_{xy}\sin(2\omega\Delta t) \tag{13}$$

$$\sigma'^{co}_{xy} = \sigma'_{xx}\sin(2\omega\Delta t) + \sigma'_{xy}\cos(2\omega\Delta t) \tag{14}$$

$$\omega = \frac{1}{2}\left(\frac{\partial v_y}{\partial x} - \frac{\partial v_x}{\partial y}\right) \tag{15}$$

where ω is the rotation rate or spin of the material [21].

A free surface is implemented in the model using a sticky-rock interface with stabilization to avoid the so called drunken sailor effect. This is achieved using the approach described by [22] whereby advection-related density changes are incorporated into (2) to better approximate density at the end of the time step and avoid the drunken sailor effect. The modified y-Stokes equation is given by:

$$-\frac{\partial \sigma'_{xx}}{\partial y} + \frac{\partial \sigma'_{xy}}{\partial x} - \frac{\partial P}{\partial y} - g_y \Delta t\left(v_x\frac{\partial \rho}{\partial x} + v_y\frac{\partial \rho}{\partial y}\right) = -\rho g_y \tag{16}$$

The algorithm describe in Appendix A is used to update the deviatoric stress tensor components on markers and solve equations (1), (2), and (7) using the non-linear visco-elasto-plastic constitutive law described in equations (4), (5) and (9).

2.1.2. Conservation of Energy

Temperature is obtained by solving the conservation of energy equation as given by:

$$\rho C_p\frac{DT}{Dt} = \frac{\partial}{\partial x}\left(k\frac{\partial T}{\partial x}\right) + \frac{\partial}{\partial y}\left(k\frac{\partial T}{\partial y}\right) + H_{rad} + H_{shear} + H_{adi} + H_{melt} + H_{exo} \tag{17}$$

where T is the temperature, C_p is the specific heat capacity, k is the thermal conductivity, H_{rad} is the radiogenic heat production term, H_{smear} is the shear heating term, H_{adi} is the adiabatic heating or cooling term, H_{melt} is a melt-processes term associated with the latent heat of melting and crystallization, H_{exo} is a serpentinization term that accounts for the heat produced from exothermic serpentinization reactions, and $\frac{DT}{Dt}$ is the substantive time temperature derivative defined as:

$$\frac{DT}{Dt} = \left(\frac{\partial T}{\partial t} + v_x\frac{\partial T}{\partial x} + v_y\frac{\partial T}{\partial y}\right) \tag{18}$$

The thermal conductivity term k in (17) is described with the following temperature-dependent model:

$$k = 358(1.0227k_{20^\circ C} - 1.882)(1.0/T_K - 0.00068) + 1.84 \tag{19}$$

where $k_{20^\circ C}$ is the thermal conductivity of the rock at 20°C, T_K is temperature in Kelvin [26]. The heat capacity term C_p in (17) is described with the following

temperature-dependent model:

$$C_p = C_{p20}\Big(0.953 + 2.29 \cdot 10^{-3} T_{\circ C} - 2.835 \cdot 10^{-6} \left(T_{\circ C}\right)^2 + 1.191 \cdot 10^{-9} \left(T_{\circ C}\right)^3\Big) \tag{20}$$

where C_{p20} is the heat capacity of the rock at $20°C$ and $T_{\circ C}$ is the temperature in $°C$ [26].

The shear heating term H_{shear} is defined using the following equation:

$$H_{shear} = \frac{\sigma'^2_{xx}}{\eta_{vp}} + \frac{\sigma'^2_{xy}}{\eta_{vp}} \tag{21}$$

where σ'_{xx} and σ'_{xy} are the deviatoric components of the stress tensor and η_{vp} is the visco-plastic effective viscosity. The adiabatic heating term H_{adi} is defined using the following equation:

$$H_{adi} = c_{adi} \frac{DP}{Dt} \tag{22}$$

where $\frac{DP}{Dt}$ is the substantive pressure derivative and c_{adi} is the adiabatic coefficient given by:

$$c_{adi} = \alpha T \tag{23}$$

where α is the thermal expansion coefficient. The substantive pressure derivative $\frac{DP}{Dt}$ is defined as:

$$\frac{DP}{Dt} = \left(\frac{dP}{dx} v_x + \frac{dP}{dy} v_y\right). \tag{24}$$

The melt-processes term H_{melt} is divided into two components:

$$H_{melt} = H_{melt,adi} + H_{melt,T} \tag{25}$$

where $H_{melt,adi}$ is the melting-related adiabatic component of the latent heat of melting associated with changes in pressure within partially molten domains and $H_{melt,T}$ is the temperature-dependent component. The adiabatic component of the latent heat of melting and the temperature-dependent components are given by:

$$H_{melt,adi} = -\rho L \frac{\partial M}{\partial P} \frac{DP}{Dt} \tag{26}$$

$$H_{melt,T} = -\rho L \frac{\partial M}{\partial T} \frac{DT}{Dt} \tag{27}$$

where L is the latent heat of melting, M is the melt fraction, and $\frac{DT}{Dt}$ is the substantive temperature derivative. The latent heat of melting term L is set equal to $400,000 J/kg$ for gabbroic and ultramafic rocks [27].

Equation (27) is included in an effective heat capacity term in the energy equation (17) to account for the temperature-dependent latent heat of melting and crystallization. The effective heat capacity term is given by:

$$C_p^{eff} = C_p + L \frac{\partial M}{\partial T} \tag{28}$$

The partial derivative $\frac{\partial M}{\partial T}$ in (28) is calculated using a finite difference approximation as follows:

$$\frac{\partial M}{\partial T} = \frac{M_{T+\Delta T,P} - M_{T-\Delta T,P}}{2\Delta T} \tag{29}$$

where $\Delta T = 1K$ and $M_{T+\Delta T,P}$ and $M_{T-\Delta T,P}$ are the melt fractions at the current pressure P and temperatures $T + \Delta T$ and $T - \Delta T$, respectively.
Similarly, equation (26) is included in an effective adiabatic coefficient term in equation (22) to account for the adiabatic component of the latent heat of melting and crystallization. The effective adiabatic coefficient term is given by:

$$c_{adi}^{eff} = c_{adi} - \rho L \frac{\partial M}{\partial P} \tag{30}$$

The partial derivative $\frac{\partial M}{\partial P}$ in (30) is calculated using a finite difference approximation as follows:

$$\frac{\partial M}{\partial P} = \frac{M_{T,P+\Delta P} - M_{T,P-\Delta P}}{2\Delta P} \tag{31}$$

where $\Delta P = 1000Pa$ and $M_{T,P+\Delta P}$ and $M_{T,P-\Delta P}$ are the melt fractions at the current temperature T and pressures $P + \Delta P$ and $P - \Delta P$, respectively. The exothermic heat production term H_{exo} associated with serpentinization is given by:

$$H_{exo} = \frac{f_{serp,inc} E}{\Delta t M_{serp}} \tag{32}$$

where $f_{serp,inc}$ is the incremental serpentinization ratio, M_{serp} is the molar volume of serpentine (m^3/mol), E is the enthalpy change (J/mol) and Δt is the time step.

The substantive time pressure derivative that appears in (22) and (26) is approximated using lithostatic pressure gradients [22] as described in the following equation:

$$\left(\frac{dP}{dx} v_x + \frac{dP}{dy} v_y\right) = \rho g_x v_x + \rho g_y v_y. \tag{33}$$

The algorithm describe in Appendix B is used to solve equation (17) where the conductive component of equation 17 is obtained by solving the purely conductive formulation of equation 17 on Eulerian grid nodes and the advective component of equation 17 is solved by advecting markers using a 4th-order Runge-Kutta scheme and correcting for subgrid changes in temperature [21].

2.2. Topography Advection, Sediment Transport and Compaction

Sediment transport is modeled on a Eulerian topography grid $(x_{topo,i}, y_{topo,i})$ where i ranges from 1 to N_{topo}, N_{topo} is the number of topography nodes and $y_{topo,i}$ is the y-coordinate of the topography at the i-th node. The spacing of the topography grid in the x-direction is denoted by Δx_t, which remains constant throughout the model domain. Prior to applying the sediment transport model, topography grid nodes are advected in the current velocity field using a 4th

order Runge-Kutta scheme and then interpolated to the original topography grid to obtain new y-coordinates of topography that track the interface between rock and the sticky-air/water layer.

Sediment transport is modeled using a diffusion equation that assumes density does not differ between sediment and bedrock and that the cohesion of bedrock is negligible as to not limit sediment supply at the surface. When applied along the topography marker chain, the sediment transport equation takes the form of the following equation:

$$\frac{\partial y_{topo}}{\partial t} = \frac{\partial}{\partial x}\left(\kappa_s \frac{\partial y_{topo}}{\partial x}\right) + R_{pelagic} \tag{34}$$

where y_{topo} is the y-coordinate of topography in the 2D model domain, κ_s is the sediment transport diffusivity, and $R_{pelagic}$ is a sediment source term that accounts for pelagic sedimentation and sediment transport in and out of the plane of the model domain. The approach described by [11] is used to define κ_s so that it includes the effects of subaerial slope diffusion, subaerial fluvial concentrative diffusional transport associated with river systems within a given drainage basin and water-depth dependent submarine slope diffusion that accounts for wave and tidal effects at shallow water depths:

$$\kappa_{s,i} = \begin{cases} \kappa_{sm} \exp\left(-\frac{W}{\lambda_{sm}}\right) & \text{if } W_i > 0 \\ \kappa_{sa} + \kappa_{fluvial,i} & \text{otherwise} \end{cases} \tag{35}$$

where W_i is water depth in m, κ_{sm} is the submarine slope diffusivity in m^2/s, λ_{sm} is the submarine diffusivity water-depth decay term in m, κ_{sa} is the subaerial slope diffusivity in m^2/s and $\kappa_{fluvial}$ is the diffusivity associated with fluvial transport processes in m^2/s. The fluvial diffusivity $\kappa_{fluvial,i}$ is described by the following equation:

$$\kappa_{fluvial,i} = R_{precip} C_{subaerial} D_{stream,i} \tag{36}$$

where R_{precip} is the precipitation rate in m/s, $C_{subaerial}$ is the subaerial transport coefficient, and $D_{stream,i}$ is the downstream distance in m between drainage divides to the left and right of node i. The downstream distance $D_{stream,i}$ essentially scales fluvial diffusivity with the size of the drainage basin. A 1D conservative finite difference method is used to solve the sediment transport equation (34) with a time step of Δt_{sed}. See Table 1 for the sediment transport model parameters used in this work.

The sediment transport equation (34) does not take into account the effects of sediment compaction and assumes that sediment density is equal to bedrock density. This assumption is equivalent to assuming that the sediment is deposited in a state of maximum compaction and that the substrate upon which new sediment is deposited does not compact. A compaction correction is applied to the topography solution at each time step of the sediment transport solver to account for deposition of sediment in a less compacted state and the

compaction of pre-existing sediment:

$$y_{topo,i} = y_{topo,trans,i} - \left[\left(H^f_{sed,i} + \Delta H^f_{sed,i}\right) - \left(H^o_{sed,i} + \Delta H^o_{sed,i}\right)\right] \tag{37}$$

where $y_{topo,trans,i}$ is the topography obtained by solving the sediment transport equation (34) at node i, $H^o_{sed,i}$ is the initial sediment thickness prior to the deposition of new sediment, $\Delta H^o_{sed,i}$ is the newly deposited sediment thickness in the zero-porosity maximum compaction state, $\Delta H^f_{sed,i}$ is the newly deposited sediment thickness in a de-compacted state and $H^f_{sed,i}$ is the initial sediment thickness compacted to a depth of $\Delta H^f_{sed,i}$. The parameter $\Delta H^o_{sed,i}$ is related to the new and old topography solutions obtained from solving (34) as follows:

$$\Delta H^o_{sed,i} = \max\left[(y^o_{topo,i} - y_{topo,trans,i}),\, 0\right]. \tag{38}$$

The newly deposited decompacted sediment thickness $\Delta H^f_{sed,i}$ is calculated by de-compacting $\Delta H^o_{sed,i}$ from an assumed depth below mudline of 12 km to 0 km using the conservation of mass and assuming that the relationship between porosity and depth in the sediment column can be described by the following equation:

$$\phi = \phi_o \exp\left(-\frac{y_{sm,max}}{\lambda_{comp}}\right) \tag{39}$$

where ϕ is the sediment porosity, ϕ_o is the initial sediment porosity at the mudline, $y_{sm,max}$ is the maximum depth below the seafloor encountered by a particle during burial and λ_{comp} is the compaction decay length [28]. A similar approach is used to obtain $H^f_{sed,i}$ whereby equation (39) is used to compact $H^o_{sed,i}$ to a depth below mudline of $\Delta H^f_{sed,i}$. With each time step of the sediment transport solver a correction is also applied to the location of sediment and sticky air/water markers whereby pre-existing sediment and sticky air/water markers are advected vertically using the compaction displacement field. Interactive tests and benchmarks of this approach can be accessed through the EarthBox.jl API [20].

The marker composition field is updated to account for erosion and sedimentation processes after the sediment transport solver and compaction correction have been applied to update the y-coordinate of topography $y_{topo,i}$. The updated topography is first interpolated at the x-coordinate x_m of marker m to determine the elevation of the topography at the marker $y_{topo,m}$. If the y-coordinate of the marker y_m is less than $y_{topo,m}$ and the marker is lithological, the marker is transformed to either a sticky-air or sticky-water marker depending on whether the marker is above or below sea level to account for erosion. If the marker is sticky-air or sticky-water and y_m is greater than $y_{topo,m}$, the marker is transformed to sediment.

For a given marker m, sediment density ρ_m, thermal conductivity k_m and heat capacity $C_{p,m}$ are updated to account for water filled porosity as described

in equation (39) using the following equations:

$$\begin{aligned} \rho_m &= (1-\phi_m)\rho_{matrix,m} + \phi_m \rho_{water}, \\ k_m &= (1-\phi_m)k_{matrix,m} + \phi_m k_{water} \\ C_{p,m} &= (1-\phi_m)C_{p,matrix,m} + \phi_m C_{p,water} \end{aligned} \tag{40}$$

where $\rho_{matrix,p}$ is the density of the rock matrix, $k_{matrix,m}$ is the thermal conductivity of the rock matrix, $C_{p,matrix,m}$ is the heat capacity of the rock matrix, ρ_{water} is the density of water, k_{water} is the thermal conductivity of water and $C_{p,water}$ is the heat capacity of water.

2.3. Melt Generation, Transport and Emplacement

The models presented in this work use a linearized equilibrium melt fraction model based on the following equation:

$$M_m = \frac{T_m - T_{solidus,m}}{T_{liquidus,m} - T_{solidus,m}} \tag{41}$$

where m is the index of the marker, M_m is the melt fraction for the marker, T_m is the temperature of the marker, $T_{solidus,m}$ is the solidus temperature of the marker, and $T_{liquidus,m}$ is the liquidus temperature of the marker [15].

The solidus temperature of markers with ultramafic composition is defined for anhydrous peridotite by the following equation:

$$T^{mantle}_{solidus} = \begin{cases} -5.1(P_{GPa})^2 + 132.9P_{GPa} + 1085.7 \text{ for } P_{GPa} \leq 8 \text{ GPa} \\ T^{8GPa}_{solidus,K03} + \frac{\left(T_{solidus20} - T^{8GPa}_{solidus,K3}\right)}{12}(P_{GPa} - 8) \text{ for } P_{GPa} > 8 \text{ GPa} \end{cases} \tag{42}$$

where P_{GPa} is the pressure in GPa, $T^{8GPa}_{solidusK3}$ is the solidus temperature in K at 8 GPa according to the model of [29], and $T_{solidus20}$ is the solidus temperature in K at 20 GPa set equal to 2250 K. Anhydrous peridotite is used as water is quickly removed from the system during the early stages of melting. The liquidus temperature for ultramafic mantle markers is defined by the following equation for anhydrous peridotite:

$$T^{mantle}_{liquidus} = \begin{cases} -2(P_{GPa})^2 + 45.0P_{GPa} + 1780.0 \text{ for } P_{GPa} \leq 8 \text{ GPa} \\ T^{8GPa}_{liquidus,K3} + \frac{\left(T_{liquidus20} - T^{8GPa}_{liquidus,K03}\right)}{12}(P_{GPa} - 8) \text{ for } P_{GPa} > 8 \text{ GPa} \end{cases} \tag{43}$$

where $T^{8GPa}_{liquidusK3}$ is the liquidus temperature in K at 8 GPa according to the model of [29], and $T_{liquidus20}$ is the liquidus temperature in K at 20 GPa set equal to 2600 K.

This study employs two models to determine the solidus and liquidus temperatures for gabbro: (1) a standard gabbro model representing the composition of primary melt products derived from the mantle, and (2) a model for gabbroic materials that have experienced fractional crystallization during emplacement.

The solidus and liquidus temperatures for markers that have normal gabbro composition are defined by the following equations from [21]:

$$\begin{aligned} T^{gabbro}_{solidus} &= 1327.0 + 91 P_{GPa}, \\ T^{gabbro}_{liquidus} &= 1423 + 105 P_{GPa} \end{aligned} \tag{44}$$

The solidus and liquidus temperatures for fractionated gabbro are defined by the following equations:

$$\begin{aligned} T^{frac}_{solidus} &= T^{gabbro}_{solidus} + \Delta T^{frac}_{solidus} \\ T^{frac}_{liquidus} &= T^{gabbro}_{liquidus} + \Delta T^{frac}_{liquidus} \end{aligned} \tag{45}$$

where $\Delta T^{frac}_{solidus}$ and $\Delta T^{frac}_{liquidus}$ are the temperature differences between the solidus and liquidus temperatures for normal gabbro and fractionated gabbro, respectively. We use the following values for fractionated shifts in solidus and liquidus temperatures based on the work of [30]: $\Delta T^{frac}_{solidus} = 100\ K$ and $\Delta T^{frac}_{liquidus} = 300\ K$.

Melt is assumed to migrate instantaneously to the top of the partially molten mantle domain and then flow horizontally toward local high points (Figure 5). This assumption is justified by laboratory measurements of permeability and melt flow rates in olivine aggregates that have been used to infer melt transport times across the entire asthenosphere of around 1000 years [31]. At the local maximum of the partially molten domain melt is divided into two fractions: one that is immediately emplaced at the base of the crust via dikes and channelized networks and another that is transported to the surface (Figure 5). This transport and emplacement model is similar to the model described by [32, 33] where melt from focusing zones in the partially molten mantle is transported to the crustal domain at the spreading axis via a melt extraction zone composed of dike swarms. This simplified model of melt transport and emplacement is implemented independently within each melt drainage basin bounded by local minima along the top of the partially molten domain.

The extractable melt fraction for a marker m is defined by the following equation:

$$M_{extractable,m} = M_m - M^o_{extracted,m} \tag{46}$$

where M_m is the total melt fraction for the marker as described in (41) and $M^o_{extracted,m}$ is the melt fraction already extracted. The extracted melt fraction is updated using:

$$M_{extracted,m} = M^o_{extracted,m} + M_{extractable,m} \text{ if } M_m > 0 \text{ and } M_{extractable,m} > 0 \tag{47}$$

Marker density ρ_m is impacted by melting by depleting the rock matrix and through the presence of melt in the pore space. The impact of depletion is modeled using the approach of [13] as described in the following equation:

$$\rho_m = \begin{cases} \rho^o_m - 3.8 M_{extracted,m} 100 & \text{if } M_{extracted,m} < 0.075 \\ \rho^o_m - (24.84 + 0.488 M_{extracted,m} 100) & \text{if } M_{extracted,m} \geq 0.075 \end{cases} \tag{48}$$

where ρ_m^o is the density of the marker prior to the update step. The effect of melt in pore space on density modeled using the following equation:

$$\begin{aligned} \rho_{melt} &= \rho_{ref,melt} + f_{eos} P_{Pa}, \\ \rho_m &= \rho_m^o (1 - M_{extractable,m}) + \rho_{melt} M_{extractable,m} \end{aligned} \tag{49}$$

where ρ_m^o is the density of the marker prior to this update step, $\rho_{ref,melt}$ is the reference density of the melt set equal to 2750 $\frac{kg}{m^3}$, $P_{Pa,m}$ is the pressure in Pa and f_{eos} is the linearized derivative of melt density with respect to pressure equal to $8.97 \cdot 10^{-8} \frac{kg}{m^3 Pa}$ derived from the Birch-Murnagham equation-of-state for anhydrous basaltic melt using $K_{to} = 20.8$ and $K_{tp} = 4.6$ [34, 35].

The total number of magma markers in drainage basin k if all extractable melt were consolidated into a single body is calculated as:

$$N_{magma,tot,k} = f_{extraction} \left(\sum_{m=0}^{N_{marker}} M_{extractable,m} + R_{melt,k}^o \right) \tag{50}$$

subject to the conditions:

$$M_m > 0, \quad M_{extractable,m} > 0 \quad \text{and} \quad x_{divide,k} < x_m < x_{divide(k+1)} \tag{51}$$

where $f_{extraction}$ is the extraction efficiency, $R_{melt,k}^o$ is the residual melt from the previous time step, $x_{divide,k}$ and $x_{divide(k+1)}$ are the x-coordinates of the left and right drainage divides for drainage basin k, respectively, and x_m is the x-coordinate of the marker. For the experiments presented in this work $f_{extraction} = 0.99$ to account for a small amount of melt retained in the mantle during transport.

The number of magma markers available for emplacement or extrusion in drainage basin k for a given time step is:

$$N_{magma,k} = int(N_{magma,tot,k}) \tag{52}$$

and the residual component used in the next time step is updated as:

$$R_{melt,k} = N_{magma,tot,k} - N_{magma,k}. \tag{53}$$

The total extractable magma volume in the drainage basin k is then:

$$V_{magma,k} = N_{magma,k} \Delta x_m \Delta y_m \tag{54}$$

where Δx_m and Δy_m are the average widths of the markers in the x and y directions, respectively.

The height of new column of crust formed if $V_{magma,k}$ is emplaced as a dike within a spreading plate is:

$$H_{mc,k} = \frac{V_{magma,k}}{v_{ext} \Delta t} \tag{55}$$

where v_{ext} is the full extension velocity and Δt is the model time step. This characteristic magmatic crust height, $H_{mc,k}$, is used to as a proxy for the efficiency of melt transport to the surface.

The number of volcanic markers that are available for extrusion on the surface as lava flows above drainage basin k is given by:

$$N_{volcanic,k} = int(f_v N_{magma,k}) \tag{56}$$

where f_v is the extrusion efficiency factor. We assume that the efficiency of melt transport to the surface correlates with the characteristic magmatic crust height $H_{mc,k}$ as described by the following equation:

$$f_v = \begin{cases} f_{v,min} & \text{for} \quad H_{mc,k} \leq H_{mc,min} \quad \text{and} \\ f_{v(max)} & \text{for} \quad H_{mc,k} \geq H_{mc,max} \quad \text{and} \\ f_{v,min} + \frac{(H_{mc,k} - H_{mc,min})}{\Delta H_{mc}} \Delta f_v & \text{for} \quad H_{mc,min} < H_{mc,k} < H_{mc,max} \end{cases} \tag{57}$$

where Δf_v is equal to $f_{v,max} - f_{v,min}$ and ΔH_{mc} is equal to $H_{mc,max} - H_{mc,min}$. For this work, $f_{v,min} = 0.06$, $H_{mc,min} = 6000m$ and $H_{mc,max} = 7500m$. Alternative scenarios for parameter $f_{v(max)}$ are explored ranging from 0.1 to 0.7. The total volume of volcanic markers $V_{vol,k}$ extruded on the surface for a given time step is:

$$V_{vol,k} = V^o_{vol,k} + N_{volcanic,k} \Delta x_m \Delta y_m. \tag{58}$$

where $V^o_{vol,k}$ is the volume of material available for extrusion from previous model times steps within the current inter-eruption period. Inter-eruption periods ranging from $12,000$ to $100,000$ years are explored for the experiments presented in this work. The number of magma markers $N_{magma,k}$ can be updated to account for volcanic material as follows:

$$N_{magma,k} = N_{magma,k} - N_{volcanic,k}. \tag{59}$$

Therefore, the volume of magma markers that are emplaced at the base of the crust is:

$$V_{magma,k} = N_{magma,k} \Delta x_m \Delta y_m. \tag{60}$$

Similar to [17], the models presented in this work approximate dike injection by replacing shallow ultramafic material with a volume of gabbroic magma equal to the current volume of magma extracted from the mantle. The approach of [17] defines a single dike for each injection event with a width controlled by extensional velocity and a height controlled by the volume of extracted gabbroic magma. Given the complex nature of dike injection and the difficulty associated with accurately predicting the location, number and size of dikes associated with each injection event, a simpler approach is used in the current work where shallow ultramafic markers within an injection zone are probabilistically selected and replaced with an equivalent volume of gabbroic magma until all extracted magma is emplaced (Figure 5).

Gabbroic magma is injected at the base of the Moho within an injection zone of width $W_{inj,k}$ that is centered on the local maximum of the partially molten domain of the mantle (Figure 5). The width of the magma injection zone $W_{inj,k}$ is calculated using the following equation:

$$W_{inj,k} = \begin{cases} \frac{V_{magma,k}}{H_{inj,limit}} & \text{for} \quad H_{inj} > H_{inj,limit} \\ W_{inj}^{char} & \text{for} \quad H_{inj} \leq H_{inj,limit} \end{cases} \tag{61}$$

where W_{inj}^{char} is the characteristic injection width, $H_{inj,limit}$ is the maximum injection height limit, and H_{inj} is the injection height defined by:

$$H_{inj} = \frac{V_{magma,k}}{W_{inj}^{char}}. \tag{62}$$

The models presented in this work used $W_{inj}^{char} = 10$ km and $H_{inj,limit} = 1$ km. Equation (61) is used to spread out dike injection and ensure that integrated injection height during an emplacement event does not become become geologically unrealistic during the emplacement of large volumes of gabbroic magma when mantle potential temperature is high.

The injection zone is divided into subdomains that are selected using a normal probability distribution centered on the local maximum of the partially molten domain of the mantle (Figure 5). The injection of gabbroic magma is implemented by replacing the shallowest ultramafic marker below the Moho within a selected subdomain with a marker that has the composition of gabbroic magma and an emplacement temperature of 1200°C. At the beginning of each time step, gabbroic magma markers that are within 2 km of the Moho are converted into fractionated gabbroic magma markers. This conversion accounts for the fractional crystallization that occurs during the emplacement of magma in the crust, including processes such as dike and sill injection and the flow of crystal mush in the so called gabbro glacier [30].

Markers undergo solidification based on their updated melt fraction M_m. The solidification process occurs as follows:

1. Solidification is modeled by transforming purely molten markers that have cooled below the liquidus temperature to a solid state.

2. Solid markers with temperatures between the solidus and liquidus temperatures are transformed to a partially molten state.

3. Partially molten markers that have cooled below the solidus are transformed to a solid state.

If the melt fraction M_m from (41) falls below the extracted melt fraction $M_{extracted,m}$ from (46) (i.e. $M_{extractable} < 0$) the marker is transformed into a refractory state. See Table 2 for the melt extraction and emplacement parameters used in this work.

2.4. Melt Extrusion and Lava Flow

Volcanic extrusion and lava flow for a given eruption time step is modeled using a cellular automata approach [36, 37, 38] where the volume of magma available for extrusion in a melt drainage basin is divided into N_{flow} flow events that extrude from a probabilistic eruption location x_e. Flow events are temporally separated by an inter-eruption period Δt_{erupt} include all melt extracted during model time steps within the inter-eruption period. At the beginning of each flow event, the current topography grid (x_{topo}, y_{topo}) is decimated to a uniform grid (x'_{topo}, y'_{topo}) with spacing $\Delta x'_{topo}$ to improve the computational performance of the cellular automata calculation. Then a decimated flow thickness grid for the flow event, (x'_{topo}, H'_{flow}), is initialized to zero thickness. Each flow is then divided into N_{pulse} pulses that laterally flow from the eruption location x_e to adjacent cells on the decimated topography grid.

The volume of volcanic material per flow V_{flow} is calculated using the following equation:

$$V_{flow} = \frac{V_{vol,k}}{N_{flow}} \tag{63}$$

where N_{flow} is given by:

$$N_{flow} = \begin{cases} int\left(\frac{V_{vol,k}}{V_{flow}^{char}}\right) & \text{for} \quad V_{vol,k} > V_{flow}^{char} \\ 1 & \text{for} \quad \text{otherwise} \end{cases} \tag{64}$$

where $V_{vol,k}$ is the total volume of volcanic material available for extrusion from the drainage basin k calculated during the melt extraction steps that occurred within the current inter-eruption period Δt_{erupt}, and V_{flow}^{char} is the characteristic volume of volcanic material per flow given by:

$$V_{flow}^{char} = \begin{cases} L_{sa} H_{res,sa} & \text{for} \quad y_{e,fc} \leq y_{sl} \quad \text{and} \\ L_{sm} H_{res,sm} & \text{for} \quad y_{e,fc} > y_{sl} \end{cases} \tag{65}$$

where L_{sa} is the characteristic subaerial flow length, $H_{res,sa}$ is the subaerial residual flow thickness, L_{sm} is the characteristic submarine flow length, and $H_{res,sm}$ is the submarine residual flow thickness, $y_{e,fc}$ is the forecasted y-coordinate of the eruption, and y_{sl} is the y-coordinate of sea level. For the experiments presented in this work lava flow occurs in a subaerial environment by shifting base level into the lithosphere.

The forecasted y-coordinate of the eruption $y_{e,fc}$ in equation (65) is determined by interpolating the y-coordinate from the decimated topography grid (x'_{topo}, y'_{topo}) at the forecasted eruption location $x_{e,fc}$ which is calculated using the following equation:

$$x_{e,fc} = x_{e,min} + \frac{W_e}{2} \tag{66}$$

where $x_{e,min}$ is the minimum x-coordinate of the eruption location given by:

$$x_{e,min} = x'_{shallow,pm} - \frac{W_e}{2} \tag{67}$$

where $x'_{shallow,pm}$ is the average x-coordinate of the shallowest partially molten mantle marker within drainage basin k calculated during melt extraction, and W_e is the width of the eruption zone set equal to 2.5 km.

Each flow is erupted on the surface at eruption location x_e calculated as a normally distributed random variable as described by the following equation:

$$x_e \sim \mathcal{N}\left(x_{e,min} + 0.5W_e,\, (0.25W_e)^2\right) \tag{68}$$

subject to the constraint:

$$x_{e,min} \leq x_e \leq x_{e,min} + W_e. \tag{69}$$

If x_e falls outside this range, it is recalculated.

Each flow is erupted in a series of pulses where the number of pulses is:

$$N_{pulse} = \max\left[int\left(\frac{V_{flow}}{\left(\Delta x'_{topo} H_{res}\right)}\right),\, 1\right] \tag{70}$$

where $\Delta x'_{topo}$ is the grid spacing of a decimated topography grid used to perform cellular automata calculations, and H_{res} is the residual flow thickness given by:

$$H_{res} = \begin{cases} H_{res,sa} & \text{for} \quad y_e \leq Y_{sl} \quad \text{and} \\ H_{res,sm} & \text{for} \quad y_e > Y_{sl} \end{cases} \tag{71}$$

The initial thickness of each pulse is calculated using the following equation:

$$H_{pulse} = \frac{V_{flow}}{N_{pulse}\Delta x'_{topo}} \tag{72}$$

A critical step in the cellular automata calculation is to sort the indices of the decimated topography grid based on the distance from the eruption location x_e with grid index given by:

$$i_e = int\left(\frac{x_e}{\Delta x'_{topo}}\right). \tag{73}$$

For a given pulse of volcanic material, the cellular automata calculation is initialized as:

$$H'_{flow(i_e)} = H'^{o}_{flow(i_e)} + H_{pulse}. \tag{74}$$

where $H'^{o}_{flow(i_e)}$ is the thickness of the flow at index i_e prior to the current pulse. For a given lava pulse, flow thickness H'_{flow} is updated for each cell by radiating outward from index i_e. Basaltic lava material flows from cells with higher relative elevation to adjacent cells with the lower relative elevation until the integrated thickness of the lava flow H'_{flow} equals the residual thickness H_{res} after which flow ceases to occur. During the iterative update procedure for a

given pulse of the lava, the y-coordinates of topography, $y''_{topo(i)}$, $y''_{topo(i-1)}$, and $y''_{topo(i+1)}$ are are related to current flow thickness $H'_{flow(i)}$ as follows:

$$\begin{aligned} y''_{topo(i)} &= y_{topo}(i)' - H'_{flow(i)} \\ y''_{topo(i-1)} &= y_{topo}(i-1)' - H'_{flow(i-1)} \\ y''_{topo(i+1)} &= y_{topo}(i+1)' - H'_{flow(i+1)} \end{aligned} \tag{75}$$

and elevation differences that drive flow from cell i to adjacent cells are given by:

$$\begin{aligned} \Delta E'_{left(i)} &= \max(0,\, y''_{topo(i-1)} - y''_{topo(i)}) \\ \Delta E'_{right(i)} &= \max(0,\, y''_{topo(i+1)} - y''_{topo(i)}). \end{aligned} \tag{76}$$

where positive values of $\Delta E'_{left(i)}$ and $\Delta E'_{right(i)}$ indicate that flow will occur from cell i to adjacent cells $i-1$ and $i+1$, respectively, if current flow thickness $H'_{flow(i)}$ is greater than the residual thickness H_{res}. The total thickness of lava available to flow to adjacent cells is given by:

$$\Delta H'_{out,total(i)} = \frac{2}{3} \min \left[\max \left(0,\, H'_{flow(i)} - H_{res} \right),\, \Delta E'_{limit(i)} \right] \tag{77}$$

where $\Delta H'_{out,total(i)}$ is the total thickness of lava available to flow from cell i to adjacent cells, and $\Delta E'_{limit(i)}$ is given by:

$$\Delta E'_{limit(i)} = \begin{cases} \left(\Delta E'_{left(i)} + \Delta E'_{right(i)} \right) / 2 & \text{if} \quad \Delta E'_{left(i)} > 0 \quad \text{and} \quad \Delta E'_{right(i))} > 0 \\ \Delta E'_{right(i)} & \text{else if} \quad \Delta E'_{right(i)} > 0 \\ \Delta E'_{left(i)} & \text{else} \quad \Delta E'_{left(i)} > 0. \end{cases} \tag{78}$$

Equation (77) facilitates convergence of the cellular automata iterations by limiting the amount of inter-cellular flow and ensuring that flow does not occur if flow thickness is less than or equal to the residual flow thickness H_{res}.

The total outflow thickness $H'_{out,total(i)}$ is partitioned to adjacent cells using the following equations:

$$\begin{aligned} \Delta H'_{out,left(i)} &= \min \left(\Delta H'_{out,total(i)} \frac{\Delta E'_{left(i)}}{\left(|\Delta E'_{left(i)}| + |\Delta E'_{right(i)}| \right)},\, \Delta E'_{left(i)} \right) \\ \Delta H'_{out,right(i)} &= \min \left(\Delta H'_{out,total(i)} \frac{\Delta E'_{right(i)}}{\left(|\Delta E'_{left(i)}| + |\Delta E'_{right(i)}| \right)},\, \Delta E'_{right(i)} \right). \end{aligned} \tag{79}$$

where outflow thickness is limited by elevation differences between cells. The thickness of the flow is updated for cell i and adjacent cells using the following

equations:

$$\begin{aligned} H'_{flow(i-1)} &= H'^{o}_{flow(i-1)} + \Delta H'_{out,left(i)} \\ H'_{flow(i)} &= H'^{o}_{flow(i)} - \Delta H'_{out,left(i)} - \Delta H'_{out,right(i)} \\ H'_{flow(i+1)} &= H'^{o}_{flow(i+1)} + \Delta H'_{out,right(i)} \end{aligned} \tag{80}$$

where $H'^{o}_{flow(i-1)}$, $H'^{o}_{flow(i)}$, and $H'^{o}_{flow(i+1)}$ are the thickness of the flow prior to the current cellular automata iteration. For each iteration of the cellular automata calculation, equations (80) are applied to each cell in the decimated topography grid. These iterations are repeated until the maximum thickness difference between iterations falls below a tolerance of 10^{-4}.

After the thickness of the flow on the decimated grid, $H'_{flow,i}$, is updated for each pulse, flow thickness is interpolated and added to the original un-decimated topography grid producing an updated flow thickness $H_{flow,i}$. The topography grid at the end of a flow event is then updated as follows:

$$y_{topo,i} = y^{o}_{topo,i} - H_{flow,i} \tag{81}$$

where $y^{o}_{topo,i}$ is y-coordinate of the topography from the prior flow event. Equation (81) ensures that lava flow calculations are consistent with a dynamically evolving landscape impacted by the flow of volcanic material.

The thickness of lava $H_{flow,i}$ produced during a given flow event is added to $H_{flow,tot,i}$, which is the integrated thickness of all flow events associated with a thermo-mechanical model time step. The total flow thickness $H_{flow,tot,i}$ is used to transform sticky markers to volcanic material if y_m is greater than $y_{topo,m}$, which is the interpolated y-coordinate of the updated topography grid $y_{topo,i}$ at x-coordinate x_m. For cases where topography has been updated for both sedimentation and extrusive flow, sticky markers are transformed to volcanic sediment if y_m is greater than $y_{topo,m} + H_{flow,tot,m}$ and to volcanic markers if y_m is less than $y_{topo,m} + H_{flow,tot,m}$ where $H_{flow,tot,m}$ is the total thickness of lava flows interpolated at the x-coordinate of the marker x_m. This approach assumes that sediment is deposited prior to the eruption of volcanic material. The current volume of volcanic material available for extrusion, $V_{vol,k}$, is reset to zero at the end of each eruption event. See Table 2 for the extrusion and lava-flow parameters used in this work.

2.5. Composite Viscous Creep

A composite rheology is used to model solid-state creep including diffusion, dislocation, and Peierls creep. The composite effective strain rate invariant $\dot{\epsilon}_{eff}$ is given by:

$$\dot{\epsilon}_{eff} = \max\left(\dot{\epsilon}_{dis}, \dot{\epsilon}_{pei}\right) + \dot{\epsilon}_{dif}. \tag{82}$$

where $\dot{\epsilon}_{dis}$, $\dot{\epsilon}_{pei}$, and $\dot{\epsilon}_{dif}$ are the strain rate invariants for dislocation, Peierls, and diffusion creep, respectively. The effective creep viscosity $\eta_{creep,m}$ is then given by:

$$\eta_{creep,m} = \frac{\sigma'_{II(m)}}{2\dot{\epsilon}_{eff}} \tag{83}$$

where $\sigma'_{II(m)}$ is the second invariant of the stress tensor in MPa.

The strain rate invariant for diffusion creep $\dot{\epsilon}_{dif}$ is calculated using the following equation:

$$\dot{\epsilon}_{dif} = A_{dif} \exp\left[-\frac{\left(E_{dif(m)}10^3 + V_{dif(m)} * P_m 10^{-6}\right)}{R_{gas} T_m}\right] (\sigma'_{II(m)} 10^{-6}) \tag{84}$$

where $A_{dif(m)}$ is the diffusion creep pre-exponential factor in $1/s/MPa$, $E_{dif(m)}$ is the diffusion creep activation energy in kJ/mol, $V_{dif(m)}$ is the diffusion creep activation volume in $J/MPa/mol$, R_{gas} is the ideal gas constant in $J/mol/K$, T_m is the marker temperature in K, and P_m is the marker pressure in Pa. The strain rate invariant for dislocation creep $\dot{\epsilon}_{dis}$ is given by:

$$\dot{\epsilon}_{dis} = A_{dis} \exp\left[-\frac{\left(E_{dis(m)}10^3 + V_{dis(m)} * P_m 10^{-6}\right)}{R_{gas} T_m}\right] (\sigma'_{II(m)} 10^{-6})^{n_m} \tag{85}$$

where A_{dis} is the dislocation creep pre-exponential factor in $1/s/(MPa)^n$, E_{dis} is the dislocation creep activation energy in kJ/mol, V_{dif} is the dislocation creep activation volume in $J/MPa/mol$ and n_m is the stress exponent. Finally, the strain rate invariant for Peierls creep $\dot{\epsilon}_{pei}$ is calculated using the following equation:

$$\dot{\epsilon}_{pei} = A_{pei} (\sigma'_{II(m)} 10^{-6})^2 \exp\left[-\frac{\left(E_{pei(m)}10^3 + V_{pei(m)} * P_m 10^{-6}\right)}{R_{gas} T_m} \left(1 - \left(\frac{\sigma'_{II(m)} 10^{-6}}{\sigma_{pei(m)}}\right)^{n1_m}\right)^{n2_m}\right] \tag{86}$$

where $A_{pei(m)}$ is the Peierls creep pre-exponential factor in $1/s/(MPa)^2$, $E_{pei(m)}$ is the Peierls creep activation energy in kJ/mol, $V_{pei(m)}$ is the Peierls creep activation volume in $J/MPa/mol$, $\sigma_{pei(m)}$ is the Peierls stress in MPa and $n1_m$ and $n2_m$ are the Peierls stress exponents. See Table 3 for the creep parameters used in this work.

The visco-elastic nature of the rheology implemented in this work and the power law and exponential nature of the creep mechanisms introduces a non-linear time-dependent relationship between stress and effective viscosity. Similar to [21] a bisection algorithm (Appendix D) is used to solve for the effective viscosity consistent with a visco-elastic stress forecast for a given marker m calculated using the following equations:

$$\begin{aligned}
f_{ve,m} &= \frac{\eta_{creep,m}}{\mu_m \Delta t + \eta_{creep,m}}, \\
\sigma'_{xx,fc,m} &= 2\eta_{creep,m} \dot{\epsilon}'_{xx,m} R_{sr,m} (1 - f_{ve,m}) + \sigma'_{xx,m} f_{ve,m}, \\
\sigma'_{xy,fc,m} &= 2\eta_{creep,m} \dot{\epsilon}'_{xy,m} R_{sr,m} (1 - f_{ve,m}) + \sigma'_{xy,m} f_{ve,m}, \\
\sigma'_{II,fc,m} &= \max\left(\sqrt{\left(\sigma'_{xx,fc,m}\right)^2 + \left(\sigma'_{xy,fc,m}\right)^2}, \sigma_{min}\right)
\end{aligned} \tag{87}$$

where σ_{min} is a user-defined minimum stress value, f_{ve} is the visco-elastic factor, μ_m is the shear modulus, Δt is the time step and $\dot{\epsilon}'_{xx,m}$ and $\dot{\epsilon}'_{xy,m}$ are the deviatoric strain rate components interpolated from strain rate defined on the staggered grid as described by equation (A.6), and $R_{sr,m}$ is strain rate ratio given by the following equation:

$$R_{sr,m} = \frac{\dot{\epsilon}'_{II,stress,m}}{\dot{\epsilon}'_{II,velocity,m}} \tag{88}$$

where $\dot{\epsilon}'_{II,velocity,m}$ is the strain rate invariant for marker m calculated using the following equation:

$$\dot{\epsilon}'_{II,velocity,m} = \sqrt{\left(\dot{\epsilon}'_{xx,m}\right)^2 + \left(\dot{\epsilon}'_{xy,m}\right)^2}. \tag{89}$$

and $\dot{\epsilon}'_{II,stress,m}$ is the strain rate invariant for marker m calculated using nodal deviatoric stress and deviatoric stress changes interpolated from the staggered grid as follows:

$$\dot{\epsilon}'_{II,stress,m} = \sqrt{\left(\frac{\sigma'_{xx,m_2}}{2\eta_{vp,m}} + \frac{\Delta\sigma'_{xx,m}}{2\Delta t\mu_m}\right)^2 + \left(\frac{\sigma'_{xy,m_2}}{2\eta_{vp,m}} + \frac{\Delta\sigma'_{xy,m}}{2\Delta t\mu_m}\right)^2} \tag{90}$$

where σ'_{xx,m_2} and σ'_{xy,m_2} are the forecasted deviatoric stress components at markers interpolated from forecasted deviatoric grid stress $\sigma'_{xx(i,j)_{p2}}$ and $\sigma'_{xy(i,j)_{b2}}$ from equation (A.7) and $\Delta\sigma'_{xx,m}$ and $\Delta\sigma'_{xy,m}$ are the grid stress changes at markers interpolated from $\Delta\sigma'_{xx(i,j)_p}$ and $\Delta\sigma'_{xy(i,j)_b}$ from equation (A.1). The use of $R_{sr,m}$ in equation (87) makes the visco-elastic stress forecast dependent on nodal stress and reduces numerical diffusion in shear zones [21].

With each time step, the effective visco-plastic viscosity $\eta_{vp,m}$ is initialized with the effective creep viscosity $\eta_{creep,m}$ before the effects of plastic failure and partial melt are taken into account using equation (9) and the following equation, respectively:

$$\begin{aligned} \eta_{vp,m} = \eta^o_{vp,m} / \exp\left(f_\alpha M_{extractable,m}\right) \quad & for \quad M_{extractable,m} < 0.3 \quad \text{and,} \\ \eta_{vp,m} = \eta_{melt} \quad & for \quad M_m \geq 0.3 \end{aligned} \tag{91}$$

where $\eta^o_{vp,m}$ is the previous visco-plastic viscosity initialized as $\eta_{creep,m}$, f_α is a user-defined parameter that controls the sensitivity of the visco-plastic viscosity to melt fraction and η_{melt} is the viscosity of melt at $M_{extractable,m} = 1$. The parameter f_α is set to 35 in this work.

2.6. Strain Weakening and Melt Damage

Experimental work shows that the yield stress in equation (12) decreases as phyllosilicate minerals and foliation form and the pressure-solution deformation mechanism becomes dominant as grain size is reduced in shear zones [39]. This weakening of frictional-plastic strength is modeled by reducing the cohesion

and friction angle with increasing plastic strain as described by the following equations:

$$\begin{aligned} \sigma_{c,m} &= \sigma^o_{c,m} + \frac{(\sigma^f_{c,m} - \sigma^o_{c,m})}{(\epsilon^f - \epsilon^o)}(\epsilon_{plastic,m} - \epsilon^o) \\ \theta_m &= \theta^o_m + \frac{(\theta^f_m - \theta^o_m)}{(\epsilon^f - \epsilon^o)}(\epsilon_{plastic,m} - \epsilon^o) \end{aligned} \tag{92}$$

where m is the index of the marker, $\epsilon_{plastic,m}$ is plastic strain of the marker, ϵ^o and ϵ^f are initial and final reference plastic strain, $\sigma^o_{c,m}$ and $\sigma^f_{c,m}$ are initial and final reference cohesion, θ^f_m is the final reference friction angle, and θ^o_m is the initial reference friction angle that is randomized at the beginning of each time step using the following equation from [9]:

$$\theta^o_m = {\theta'_m}^o + (0.5 - r) f_{random} \tag{93}$$

where ${\theta'_m}^o$ is the initial reference friction angle of the material associated with marker m, r is a random number in the range [0,1], and f_{random} is a randomization factor controlling the magnitude of the perturbation and set equal to 10 for the experiments of this work. The randomization of friction angles described in equation (93) is used to model the evolving variability of frictional-plastic strength due to fluid-rock interactions [9]. The final reference friction angle θ^f_m is defined as:

$$\theta^f_m = \frac{{\theta'_m}^f}{{\theta'_m}^o}\theta^o_m \tag{94}$$

where ${\theta'_m}^f$ is the unmodified final reference friction angle of the material associated with marker m. Marker plastic strain $\epsilon_{plastic,m}$ in equation (92) is calculated using the following equations:

$$\begin{aligned} \sigma'_{II,m} &= \sqrt{\left(\sigma'_{xx,m}\right)^2 + \left(\sigma'_{xy,m}\right)^2}, \\ \dot{\epsilon}_{plastic,m} &= \frac{1}{2}\sigma'_{II,m}\left(\frac{1}{\eta_{vp,m}} - \frac{1}{\eta_{creep,m}}\right), \\ \epsilon_{plastic,m} &= \epsilon^o_{plastic,m} + (\dot{\epsilon}_{plastic,m}\Delta t - \dot{\epsilon}_{healing}\Delta t) \end{aligned} \tag{95}$$

where $\epsilon^o_{plastic,m}$ is the current marker plastic strain, $\dot{\epsilon}_{plastic,m}$ is the plastic strain rate, $\sigma'_{II,m}$ is the second invariant of the stress tensor, and $\dot{\epsilon}_{healing}$ is the plastic healing rate. See Table 4 for the strain weakening parameters used in this work.

As melt is transported through the melt extraction zone in lithosphere [32, 33] it can weaken the bulk frictional-plastic yield strength by forming pressurized dike swarms that may be weaker than the surrounding rock prior to solidification and by forming reactive channelized networks. In this work weakening associated with melt transport is assumed to occur in the melt-damage zone located within the melt-extraction zone and above local maxima of the partially molten domain in the mantle (Figure 5). The maximum probability of melt damage for a given marker m is assumed to scale with amount of melt being generated in a melt drainage basin k, which is defined by the characteristic

magmatic crust height $H_{mc,k}$ calculated during melt extraction (see equation (55)). The weakening from damage associated with melt transport is modeled by reducing cohesion and friction angle based on a melt damage factor $f_{damage,m}$ as described by the following equations:

$$\begin{aligned} \sigma_{c,m} &= \frac{\sigma_{c,m}}{f_{damage,m}}, \\ \theta_m &= \frac{\theta_m}{f_{damage,m}}. \end{aligned} \tag{96}$$

The melt damage factor $f_{damage,m}$ is defined in a binary manner where $f_{damage,m}$ is set equal to 1 outside of the melt damage zone and set equal to either 1 or a constant value greater than 1 based on a probability distribution within the melt damage zone. A melt damage zone is defined for a given melt drainage basin k by the x-coordinate limits x^{min}_{damage} and x^{max}_{damage} and y-coordinate limit y^{max}_{damage} defined as follows:

$$\begin{aligned} x^{min}_{damage} &= x'_{shallow,pm,k} - \frac{W_{damage}}{2}, \\ x^{max}_{damage} &= x'_{shallow,pm,k} + \frac{W_{damage}}{2}, \\ y^{max}_{damage} &= y'_{shallow,pm,k} \end{aligned} \tag{97}$$

where $x'_{shallow,pm,k}$ is the average x-coordinate of the shallowest partially molten mantle marker and $y'_{shallow,pm,k}$ is the average y-coordinate of the shallowest partially molten mantle marker calculated during melt extraction, and W_{damage} is the width of the damage zone set equal to values ranging from 1.25 to 10 km for the experiments presented in this work. The melt-damage model is applied to each marker m in the melt damage zone excluding sticky-air and sticky-water markers.

The melt damage factor $f_{damage,m}$ for a given marker m is calculated using the following equation:

$$f_{damage,m} = \begin{cases} f_{damage,max} & \text{if } r < p_{damage,m} \\ 1.0 & \text{if } r \geq p_{damage,m} \end{cases} \tag{98}$$

where $f_{damage,max}$ is the maximum melt damage factor set equal to values ranging from 1 to 10 for the experiments of this work, and r is a random number between 0 and 1. The damage probability $p_{damage,m}$ is calculated using the following equation:

$$p_{damage,m} = \begin{cases} 0.0 & \text{if } x^{max}_{damage} < x_m < x^{min}_{damage} \\ \left[\frac{p^{central}_{damage}}{2\cos\left(\frac{\left(x_m - x'_{shallow,pm,k}\right)}{W_{damage}} 2\pi \right) + 1} \right] & \text{if } x^{min}_{damage} \leq x_m \leq x^{max}_{damage} \end{cases} \tag{99}$$

where the central damage zone damage probability $p_{damage}^{central}$ is given by:

$$p_{damage}^{central} = \begin{cases} 0.0 & \text{if } H_{mc,k} \leq H_{mc,min} \\ p_{damage}^{max} & \text{if } H_{mc,k} \geq H_{mc,max} \\ \frac{p_{damage}^{inter}}{H_{mc,inter} - H_{mc,min}} \Delta H_1 & \text{if } H_{mc,min} < H_{mc,k} \leq H_{mc,inter} \\ p_{damage}^{inter} + \frac{p_{damage}^{max} - p_{damage}^{inter}}{H_{mc,max} - H_{mc,inter}} \Delta H_2 & \text{if } H_{mc,inter} < H_{mc,k} < H_{mc,max} \end{cases} \tag{100}$$

where $\Delta H_1 = (H_{mc,k} - H_{mc,min})$, $\Delta H_2 = (H_{mc,k} - H_{mc,inter})$, $H_{mc,k}$ is characteristic magmatic crust height for drainage basin k calculated during melt extraction, $H_{mc,min}$ is the minimum reference characteristic magmatic crust height, $H_{mc,max}$ is the maximum reference characteristic magmatic crust height, $H_{mc,inter}$ is the intermediate reference characteristic magmatic crust height, p_{damage}^{max} is the maximum damage probability, and p_{damage}^{inter} is the intermediate damage probability. See Table 5 for the melt damage parameters used in this work.

3. Model Setup

The model domain has dimensions 500 km by 160 km and is initialized with a 10 km thick sticky air layer, a 22 km thick felsic upper continental crust layer approximated as wet quartzite, a 13 km thick mafic lower continental crust layer approximated as wet anorthite and a 90 km thick ultramafic continental mantle lithosphere layer superimposed on an ultramafic asthenosphere layer (Figure 2). Similar to [9], lateral strong zones where strain weakening is disabled are used to localize deformation in the central part of the model domain. See Table 6 for the material properties associated with each layer. The initial thermal structure is defined using an analytical 1D model with a constant temperature at the base of the continental lithosphere that takes into account a thermal anomaly ΔT_1 and thermal properties from Table 6. The initial thermal structure within the asthenosphere is calculated using an adiabatic gradient of $0.4°C/km$.

The temperature boundary condition along the top of the model domain is set to a constant temperature of $0°C$, and the side boundaries have a zero heat flux boundary condition. The temperature boundary condition at the base of the model is defined using the following equation:

$$T_{base} = T_{lith} + \gamma L_{asthenosphere} \tag{101}$$

where T_{lith} is the temperature at the base of the continental lithosphere, γ is the adiabatic gradient in $°C/km$, and $L_{asthenosphere}$ is the thickness of the asthenosphere in km. For the models presented in this work $\gamma = 0.4°C/km$ and $L_{asthenosphere} = 25$ km. At the start of the model $T_{lith} = T_{lith,steady} + \Delta T_1$ where $T_{lith,steady}$ is the background unperturbed temperature at the base of the continental lithosphere and ΔT_1 is the thermal anomaly associated with a plume that rapidly ascends through the asthenosphere and spreads out laterally beneath the continental lithosphere. After $1Myr$ the thermal anomaly ΔT_1 is set

to zero, T_{lith} is equal to an unperturbed temperature $T_{lith,steady}$ and the bottom temperature is recomputed using equation (101). For the models presented in this work, $T_{lith,steady} = 1345°C$ and ΔT_1 is set to a range of values from $50°C$ to $150°C$ (Figure 2). This simple transient boundary condition approach provides a close approximation to the pre-rift thermal structure produced by models that include an ascending plume and significantly reduced the computational cost of the models.

Velocity boundary conditions along the side boundaries are set to outflow boundary conditions equal to $0.5v_{ext}$ where v_{ext} is a full extensional velocity of 2 cm/yr. This value of 2 cm/yr is typical of the extensional velocity inferred from continental plate reconstruction during the early phases of basin formation [7]. Prescribed inflow velocities along the top and bottom boundaries are defined so that the net inflow/outflow volume is zero over the entire model domain and the net inflow/outflow volume is zero within the sticky-air layer. The prescribed inflow velocity along the top boundary v_y^{top} is calculated as:

$$v_y^{top} = \frac{v_{ext}\left(H_{sticky,l} + H_{sticky,r}\right)}{x_{size}} \tag{102}$$

where $H_{sticky,l}$ and $H_{sticky,r}$ are the thickness of the sticky layer on the left and right sides of the model domain, and x_{size} is the width of the model domain. The prescribed inflow velocity along the bottom boundary v_y^{bot} is calculated as:

$$v_y^{bot} = v_y^{top} - 2v_{ext}\frac{y_{size}}{x_{size}} \tag{103}$$

where y_{size} is the height of the model domain (Figure 2). Inflow velocities v_y^{top} and v_y^{bot} are recalculated at each time step to account for changes in the sticky layer thickness due to crustal thickness changes and isostatic adjustment.

4. Results

A systematic exploration of parameter space associated with the melting model was conducted using 37 high-resolution model runs to explore magmatic crust formation and the development of dipping lava-flow packages (Table 7). The model parameters varied include: (1) the thermal anomaly ΔT_1 (50–150 K), which controls the total volume of melt produced during the model run; (2) the maximum extrusion factor $f_{v,max}$ (0.10–0.70), which determines the fraction of melt that can reach the surface as subaerial flows; (3) the half-width of the melt damage zone $0.5W_{damage}$ (625–5000 m), which controls the spatial extent of probabilistic melt damage weakening; (4) the maximum melt damage factor $f_{damage,max}$ (1.0–10.0), which defines the magnitude of the reduction of friction coefficients and cohesion in the melt-damage zone; (5) the characteristic length of subaerial flows L_{sa} (10,000–100,000 m), which influences how far subaerial flows can extend beyond the eruption location; and (6) the inter-eruption period Δt_{erupt} (12,500–100,000 yr), which controls the integrated volume of lava associated with eruption events.

4.1. Base Case: Magmatic Crust Formation with Melt Damage

This base case model (Case 0, Figure 3) uses the following parameters: $\Delta T_1 = 100$ K, $f_{v,max} = 0.50$, $0.5W_{damage} = 2500$ m, $f_{damage,max} = 10.0$, $L_{sa} = 20,000$ m, and $\Delta t_{erupt} = 50,000$ yr. Early in the model run, lava flowed preferentially to the left conjugate plate due to a rift flank in the lava-flow packages on the right conjugate plate (Figure 3h). Flow packages as defined here are composed of multiple individual flows and can exceed the characteristic length of a single subaerial flow. This asymmetry in flow direction led to 1-2 km greater total lava flow thickness and larger dips of flow packages on the left conjugate (Figure 4a). The left conjugate margin exhibits continuous seaward-dipping flow packages with lengths ranging from 20 to 40 km superimposed on faulted blocks composed of seaward-dipping flow packages with lengths ranging from 10 to 20 km. Subaerial flow packages on the left-conjugate plate show a range of dips from a 1° to 3° close to the spreading axis to 20° to 40° in the proximal setting where greater spreading and burial leads to increased rotation (Figures 3 and 4a).

The right conjugate plate displays fault blocks composed predominantly of seaward-dipping flows (Figure 3 and 4a). More symmetric seaward-dipping flows develop on both conjugates plate as the system evolves toward equilibrium spreading. The total volcanic flow thickness increases systematically away from the spreading axis, ranging from approximately 2 km near the axis to greater than 5 km in the proximal domain. The gabbroic basement beneath the volcanic sequences exhibits minor relief with amplitudes less than 500 m associated with localized faulting at the spreading axis.

4.2. The Critical Role of Probabilistic Melt Damage

The importance of the probabilistic melt damage mechanism is illustrated by comparing Case 0 with Case 9 (Figure 5), which uses no melt damage (i.e. $f_{damage,max} = 1.0$ versus 10.0). Without the localizing effects of melt damage longer-wavelength graben develop in flow packages and accumulate thick packages of lava that drive ductile flow in the hot and accreting gabbroic crust. Faulting is complex and polyphase and coupled with a mobile gabbro substrate that produces both seaward and landward dipping flow packages (Figure 5d, e and f) and large ridges of gabbroic crust (Figure 5).

4.3. Effect of Maximum Melt Damage Factor

The maximum melt-damage factor $f_{damage,max}$ exerts a strong control on both the volcanic architecture and basement structure (Figure 6). When the melt-damage factor is below 1.5 high-amplitude gabbroic ridges develop with a similar geometry to Case 9, reflecting insufficient localization of deformation at the spreading axis to stabilize spreading (Figure 5a). With intermediate values of the melt-damage factor (1.5 to 3) the basement relief decreases but remains more prominent than in the base case (Figure 5b). When the melt-damage factor is greater than 4, lava-flow-package geometry and magmatic structure structure is similar to the base case with relatively smooth basement and well-developed seaward-dipping flow packages (Figure 5c).

4.4. Effect of Melt Damage Zone Width

The width of the melt damage zone W_{damage} also exerts a strong control on magmatic crust evolution and the configuration of lava-flow-packages (Figure 7). A narrow melt-damage zone ($W_{damage} < 1000$ m) produces results that are similar to Case 9, with moderate-amplitude gabbroic ridges and complex flow-package geometries including both landward and seaward-dipping flow packages (Figure 7a). Intermediate melt-damage-zone widths (2000 m to 3000 m) produce results that are similar to the base case (Figure 3) but with more symmetric conjugate seaward-dipping packages and more symmetry in conjugate total flow thickness (Figure 7b). Wide melt-damage zones (3000 m to 5000 m) produce results nearly identical to the base case (Figure 7c).

4.5. Effect of Inter-Eruption Period

Increasing the inter-eruption period from 50,000 yr to 100,000 yr (Figures 8 and 9) produces symmetric and smooth divergent seaward-dipping flow packages with upward convexity and enhanced conjugate symmetry compared to the base case. Localized deformation along the spreading axis divides flows into conjugate packages that rotate due to spreading resulting in an axial depression that is filled by subsequent flows (Figure 9a and b). As spreading continues older seaward-dipping flows become progressively buried and rotated (Figure 9a-c). Furthermore, the gabbroic basement surface is exceptionally smooth and uniform, with minor relief associated with axial faulting compared to Case 9 (Figure 5).

4.6. Effect of Maximum Extrusion Factor

The effect of maximum extrusion factor is explored using models with a 100,000 yr inter-eruption period (Figure 8) that produces divergent and symmetric seaward-dipping lava-flow packages with upward convexity. The maximum extrusion factor ($f_{v,max}$) controls the ratio of intrusive vs extrusive crustal volume (Figure 10) and the change in total lava-flow thickness and gabbroic magmatic crust thickness away from the spreading axis. At low maximum extrusion factors ($f_{v,max} < 0.12$) the total lava-flow thickness ranges from 1–1.25 km and the layer of volcanic material exhibits uniform thickness across the magmatic crustal system (Figure 10a). When the maximum extrusion factor exceeds 0.15 total lava-flow thickness increases away from the spreading axis (Figure 10b). With maximum extrusion factors that exceed 0.25 the change in the total lava-flow thickness away from the spreading axis becomes more pronounced and the thickness of the gabbroic magmatic crust decreases away from the spreading axis by up to a factor of 2 (Figure 10c and d). Additionally, the amplitude of the axial depression caused by the separation of subaerial flow packages during spreading (Figure 10a-d).

4.7. Effect of Thermal Anomaly

The thermal anomaly ΔT_1 controls the initial temperature of the sub-lithospheric mantle and the total volume of melt produced during the model run. Lower thermal anomalies produce structures similar to Case 0 (Figure 4a) but with reduced total lava thickness (Figure 4b and c). Higher thermal anomalies produce progressively greater total lava thickness and temporally evolving flow directions that lead to asymmetric dipping flow packages and more complex geometry in the gabbroic basement (Figure 4d and e).

4.8. Effect of Characteristic Subaerial Flow Length

The characteristic length of subaerial flows L_{sa} influences the lateral extent of volcanic construction and the distribution of volcanic material across the margin (Figure 11). Short flow lengths ($L_{sa} = 10,000$ m) result in volcanic material concentrated near the spreading axis that produce pronounced axial volcanic ridges or flanks (Figure 11a). Longer flow lengths enable volcanic material to spread more broadly, creating larger volumes of thick symmetric seaward-dipping reflector packages on both conjugate plates, enhancing the rotation of older buried flows (Figure 11b-d).

5. Discussion and Conclusions

This study presents the first systematic investigation of SDR formation using high-resolution visco-elasto-plastic geodynamic models that couple mantle melting, magma transport, and extrusive lava flow emplacement. A methodological advance presented in this work is the probabilistic melt-damage weakening model that approximates the effects of melt networks, elevated melt pressures, and dike injection on lithospheric rheology. The melt-damage-model, which is both spatially and temporally coupled to active melting processes, is essential for stabilizing the spreading axis during magmatic crust formation and producing seaward-dipping flow geometries and magmatic crustal structures consistent with interpretations from seismic reflection data [1, 2, 3, 4]. An additional methodological advance is the integration of long-time-scale lithospheric deformation models with short-time-scale lava-flow emplacement models based on a cellular automata approach that includes subaerial vs submarine lava-flow conditions and episodic subaerial eruptions temporally separated by an inter-eruption period, which this study demonstrates is important for modeling the geometry of lava-flow packages and magmatic crust structure.

Cases presented in this work that use probabilistic melt-damage in the melt-extraction zone show lava-flow package dips, flow-package lengths, and total flow thickness consistent with detailed measurements of SDR geometry from offshore Brazil and Argentina based on 22,000 km of high-quality seismic data [4]. For example, modeling results generally show seaward dipping flow packages with dips less than 30° (Figure 4a) except for cases with large extrusion factors where dip may exceed 40° in the down-dip direction (Figure 10d). Additionally, the maximum total flow thickness observed in modeling results is around 7 km,

consistent with less than 15 km total thickness reported for Type II SDRs from offshore Brazil and Argentina [4].

The systematic parameter space exploration conducted in this study reveals several key controls on SDR architecture. The maximum melt damage factor ($f_{damage,max}$) and the width of the melt damage zone (W_{damage}) both exert strong controls on basement structure and volcanic architecture, with intermediate values required to produce smooth gabbroic basement and well-developed seaward-dipping flow packages (Figures 6 and 7). The inter-eruption period (Δt_{erupt}) also controls the symmetry and smoothness of dipping lava-flow packages, with longer inter-eruption periods (100,000 yr) producing more symmetric flows with smoother upward convexity compared to shorter intervals (Figures 3 and 8). The maximum extrusion factor ($f_{v,max}$) controls the ratio of extrusive to intrusive crustal volume and the total thickness of lava-flow packages, with higher values producing progressively thicker dipping lava-flow packages, a larger increase in total lava-flow thickness away from the ridge, a larger decrease in gabbroic magmatic crustal thickness away from the ridge and more pronounced axial depressions caused by spreading and separation of subaerial flows (Figures 10). Furthermore, very high thermal anomalies can produce flow direction asymmetries leading to complex basement geometries and asymmetries in conjugate dipping flow packages and magmatic crustal structures (Figure 4).

The numerical models presented in this work demonstrate the geodynamic plausibility of the SDR formation model from [3] where originally sub-horizontal subaerial lava flows are rotated due to magmatic crustal spreading and progressive burial and loading from younger flows (i.e. Type II SDRs from [4]). The models from this work show that individual flow packages undergo two phases of rotation: (1) initial rotation occurs as flow packages separate into conjugate segments during spreading, producing an axial depression that is filled by subsequent flows, and (2) subsequent rotation occurs due to progressive burial and loading from younger flows, similar to the model from [3] (Figure 9).

Several conceptual models explain the formation of SDRs using syn-kinematic emplacement of lava-flow packages during ductile flow of gabbroic magmatic crust [2, 8]. Although we cannot rule out these mobile substrate models, the numerical experiments presented in this work suggest that this mechanism is likely not associated with simple symmetric SDRs since complex lava-flow geometries including both seaward and landward dipping flows were observed when the hot accreting gabbroic substrate becomes mobile in response to loading from volcanic flows (Figure 5).

The kinematic-dynamic numerical models with a half-spreading configuration from [18, 19] use dike solidification to drive early SDR rotation. The model setup chosen by [18, 19] did successfully reproduce several key geometric features of Type II SDRs including upward convexity and divergent reflector packages similar to the results form cases 18 and 29-30 with 100,000 yr inter-eruption period from this study. The models presented in this work did not include the dike solidification and, therefore, cannot be used to assess the importance of this mechanism on early SDR rotation. However, the models presented in this work show that the early rotation of initially horizontal flows can be explained

by the separation of lava-flow packages during magmatic spreading without the need for dike solidification. It is recommended that future work explore the importance of dike solidification on early SDR rotation in the context of fully dynamic and coupled models.

Another proposed mechanism for SDR formation is the syn-kinematic emplacement of lava-flow packages in extensional basins formed by the stretching of continental crust [1, 4]. The numerical experiments presented in this work do show syn-kinematic emplacement of lava-flow packages in extending crust, but lava flow dip directions are predicted to be primarily landward for the chosen boundary conditions and initial conditions (e.g. Figure 6). This result suggests that the crustal extension mechanism would not consistently produce seaward-dipping flows and would instead produce dips in both seaward and landward directions. Future modeling work should explore this mechanism more fully by applying the melting and extrusion methods presented in this work with a wider range of initial conditions and boundary conditions including polyphase extension that captures the natural variability of volcanic margins.

The numerical models presented in this work support the use of SDRs as indicators of subaerial conditions in paleogeographic reconstructions, and suggest that the early basin-forming periods of many global plate reconstructions need to be revised [7]. Furthermore, the models provide a quantitative framework for testing hypotheses about the thermal evolution of the deep interior. The numerical experiments presented in this work support the conceptual model of [3] where SDRs are underlain by large volumes of mafic magmatic crust. This indicates that potential temperatures were sufficiently high for millions of years during the early phases of basin formation to produce large volumes of mafic melt. The preservation of thick symmetric SDR packages at many margins around the globe may indicate that thermal anomalies of 50 to 125$^{\circ}C$ were present in the sub-continental asthenosphere for several million years during the early basin-forming period.

The results presented in this work provide an example of how short-time-scale extrusive processes can be integrated with long-time-scale geodynamic processes to more fully link geodynamic model results to geologic observations. However, producing models that can reproduce additional second- and third-order details observed in seismic data may require higher spatial and temporal resolution than the models presented in this work. Future work should explore the implications of sub-200 m spatial resolution on magmatic crust evolution and lava-flow package geometries. Additionally, the patterns of SDRs are most likely sensitive to variable extension rates during basin formation often inferred from detailed plate reconstructions [7] and base level variations that introduce the effects of water on lava flow dynamics [4]. The methods presented in this work are well suited to investigate the effects of these factors on SDR architecture and the structural evolution of magmatic crust and should be explored in future modeling work.

While the 2D models presented in this work successfully reproduce first-order SDR characteristics, seismic observations reveal significant 3D variability in magmatic crust and SDR packages along strike at many margins [1, 2, 3, 4, 5, 6].

These along-strike variations, which likely reflect segmentation in mantle melting and magma transport, cannot be adequately captured by 2D models. Future work should therefore integrate the coupled melting, melt-damage, and lava flow emplacement methods introduced here with 3D geodynamic models with realistic rheology and boundary conditions consistent with plate reconstructions. Such 3D models would enable investigation of along-strike variations in thermal structure, melt generation, magma transport, and lava extrusion, and would provide a more complete framework for comparing model predictions with seismic observations at volcanic rifted margins.

Data Availability Statement

The geodynamic model code, input files for all cases and plotting tools are available on GitHub at https://github.com/eakneller/EarthBox.jl. Models in the GitHub repository are setup using lower resolution for the grids and markers so the user will have to adjust the resolution to reproduce the results in this paper.

Declaration of Competing Interest

The author declares that there are no known competing financial interests or personal relationships that could have appeared to influence the work reported in this paper.

Funding

This research did not receive any specific grant from funding agencies in the public, commercial, or not-for-profit sectors. The work was supported by Geonomy Labs.

Acknowledgments

The author would like to thank the Julia community for their contributions to scientific computing and willingness to help through community forums. The author would also like to acknowledge the work of Taras Gerya that has made extensible and versatile geodynamic modeling methods more accessible to the geoscience community.

Tables

Parameter	Symbol	Units	Value
Subaerial Transport coefficient	$C_{subaerial}$	-	10^{-4}
Subaerial slope diffusivity	$\kappa^{slope}_{submarine}$	m^2/yr	0.25
Submarine slope diffusivity	$\kappa^{slope}_{submarine}$	m^2/yr	100
Submarine diffusion decay depth	$\lambda_{submarine}$	m	1000
Precipitation rate	R_{precip}	m/yr	1.0
Pelagic sedimentation rate	$R_{pelagic}$	mm/yr	0.0
Initial porosity of sediment at mudline	ϕ_o	-	0.4
Sediment porosity decay depth	λ_ϕ	m	2500

Table 1: Sediment transport model parameters.

Parameter	Symbol	Units	Value
Extraction efficiency factor	$f_{extraction}$	-	0.99
Characteristic injection width	W_{inj}^{char}	km	10
Injection height limit	$H_{inj,limit}$	m	1000
Minimum extrusion efficiency factor	$f_{v,min}$	-	0.06
Maximum extrusion efficiency factor	$f_{v,max}$	-	0.1 0.2 0.3 0.4 **0.5** 0.6 0.7
Minimum reference characteristic magmatic crust thickness	$H_{mc,min}$	m	6000
Maximum reference characteristic magmatic crust thickness	$H_{mc,max}$	m	7500
Eruption interval	Δt_{erupt}	yr	12,500 25,000 **50,000** 100,000
Characteristic length of submarine flows	L_{sm}	km	2
Characteristic length of subaerial flows	L_{sa}	km	10 **20** 40 50 80 100
Residual thickness of submarine flows	$H_{res,sm}$	m	30
Residual thickness of subaerial flows	$H_{res,sa}$	m	30
Minimum width of eruption domain	$W_{e,min}$	m	2500
Maximum width of eruption domain	$W_{e,max}$	m	2500

Table 2: Melt extraction, emplacement and extrusion model parameters. Bold font indicate a parameter used in case 0, the base case model.

Parameter	Symbol	Units	Wet Quartzite [a]	Wet Anorthite [b]	Dry Olivine [c,d]
Dislocation Creep					
Tensor Invariant Pre-exponential Factor	A_{dis}	$s^{-1}MPa^{-n}$	8.57e-4	3.57e+3	6.51e+5
Stress Exponent	n_{dis}		4	3	3.5
Activation Energy	E_{dis}	kJ/mol	223	345	530
Activation Volume	V_{dis}	J/MPa/mol	0	38	13
Diffusion Creep					
Tensor Invariant Pre-exponential Factor	A_{dif}	$s^{-1}MPa^{-1}$			1.04e-2
Diffusion Creep Activation Energy	E_{dif}	kJ/mol			375
Diffusion Creep Activation Volume	V_{dif}	J/MPa/mol			6
Peierls Creep					
Tensor Invariant Pre-exponential Factor	A_{pei}	$s^{-m1}MPa^{-m2}$			2.5e+7
Stress Exponent $m1$	$m1_{pei}$				1
Stress Exponent $m2$	$m2_{pei}$				2
Peierls Stress	σ_{pei}	MPa			9100

Table 3: Viscous flow law parameters. Grain size is assumed to be 6 mm. Sources: a: [40], b: [41], c: [42], d: [43]

Parameter	Symbol	Units	Value
Initial reference friction angle	$\theta_m'^o$	degrees	30 [a]
Final reference friction angle	$\theta_m'^f$	degrees	7 [b]
Initial reference cohesion	$\sigma_{c,m}^o$	MPa	20 [a]
Final reference cohesion	$\sigma_{c,m}^f$	MPa	10 [a]
Initial reference plastic strain	ϵ_m^o	-	0
Final reference plastic strain	ϵ_m^f	-	1.0

Table 4: Plastic failure parameters for markers. Sources: a: [9]: [39]

Parameter	Symbol	Units	Value
Maximum melt damage factor	$f_{damage,max}$	-	1, 1.25, 2.5, 5, **10**
Width of melt damage zone	W_{damage}	m	1250.0, 2500, **5000**, 10000
Intermediate damage probability	p_{damage}^{inter}	-	0.1
Maximum damage probability	p_{damage}^{max}	-	0.8
Minimum reference magmatic crust height	$H_{mc,min}$	m	750
Intermediate reference magmatic crust height	$H_{mc,inter}$	m	2000
Maximum reference magmatic crust height	$H_{mc,max}$	m	3000

Table 5: Melt damage model parameters. Bold font indicate a parameter used in case 0, the base case model.

	Standard Density (kg/m^3)	Thermal Expansivity (1/K)	Compressibility (1/Pa)	Shear Modulus (Pa)	Reference Heat Capacity (J/kg/K)	Reference Thermal Conductivity (W/m/K)	Radiogenic Heat Production (W/m^3)	Flow Law
Sticky Air [a]	1.0 [a]	0.0	0.0	1.0e+20 [a]	100.0 [a]	200.0 [a]	0.0	Isoviscous: $10^{18}\ Pa \cdot s$
Clastic Sediment [b]	2710 [b]	3e-05	1.8e-11 [d]	3.6e+10 [d]	890 [b]	2.3 [b]	1.4e-6 [b]	Wet Quartzite
Felsic Continental Crust	2860 [c]	3e-05	1.8e-11 [d]	3.6e+10 [d]	800 [b]	2.5 [b]	1.8e-6 [b]	Wet Quartzite
Mafic Continental Crust	2900 [c]	3e-05	1.6e-11 [c]	4e+10	800 [b]	2.5 [b]	0.5e-6 [b]	Wet Anorthite
Ultramafic Continental Lithosphere	3291 [d]	3e-05	7.9e-12 [e]	6.6e+10 [e]	800 [b]	4 [b]	0	Dry Olivine
Ultramafic Asthenosphere	3311 [d]	3e-05	7.9e-12 [e]	6.6e+10 [e]	800 [b]	4 [b]	0	Dry Olivine
Gabbroic Crust	2900 [d]	3e-05	1.6e-11 [d]	4e+10	800 [b]	2.5 [b]	0	Wet Anorthite
Gabbroic Magma	2750 [f]	3e-05	1.6e-11 [d]	1e+11	800 [b]	2.5 [b]	0	Isoviscous
Fractionated Gabbroic Crust	2900 [d]	3e-05	1.6e-11 [d]	4e+10	800 [b]	2.5 [b]	0	Wet Anorthite
Fractionated Gabbroic Magma	2750 [f]	3e-05	1.6e-11 [d]	1e+11	800 [b]	2.5 [b]	0	Isoviscous

Table 6: Material properties. Sources: a: [21], b: [26], c: [13], d: [44], e: [27], f: [34]

Case	ΔT_1 (K)	$f_{v,max}$	$0.5W_{damage}$ (m)	$f_{damage,max}$	L_{sa} (m)	Δt_{erupt} (yr)	Extrusive and Intrusive Geometries
0	100	0.50	2500.0	10.0	20000	50000	left conjugate: asymmetric seaward-dipping flows superimposed on faulted lava-flow blocks; right conjugate: fault blocks composed of predominately seaward-dipping flows; subaerial flows move predominately to the left conjugate; symmetric seaward-dipping flows develop during later equilibrium spreading; total flow thickness increases away from spreading axis from 2 to > 5km; minor rugosity along the gabbroic basement with amplitude less than 500 m
1	50	0.50	2500.0	10.0	20000	50000	predominately seaward-dipping flows with maximum flow thickness < 2.5 km;
2	75	0.50	2500.0	10.0	20000	50000	similar to case0 but with less total lava thickness
3	125	0.50	2500.0	10.0	20000	50000	similar to case0 but with greater total lava thickness
4	150	0.50	2500.0	10.0	20000	50000	similar to case 0 but with greater total lava thickness
5	100	0.50	2500.0	10.0	10000	50000	similar to case 0 but with pronounced axial flanks.
6	100	0.50	2500.0	10.0	40000	50000	similar to case 0 but with larger volume of thick symmetric seaward-dipping reflector packages on both conjugates; subaerial flow associated with dipping reflectors extend onto the extended continental crust
7	100	0.50	2500.0	10.0	80000	50000	similar to case 6
8	100	0.50	2500.0	10.0	100000	50000	similar to case 6
9	100	0.50	2500.0	1.0	20000	50000	asymmetric landward and seaward dipping flow packages; large graben structures with total flow thickness exceeding 7 km; gabbroic basement composed of high-amplitude ridges
10	100	0.50	2500.0	1.2	20000	50000	similar to case 9 with high-amplitude gabbroic ridges
11	100	0.50	2500.0	2.5	20000	50000	Similar to case 0 but with more basement rugosity
12	100	0.50	2500.0	5.0	20000	50000	Similar to case 0
13	100	0.50	625.0	10.0	20000	50000	similar to case 9 with moderate amplitude gabbroic ridges
14	100	0.50	1250.0	10.0	20000	50000	symmetric seaward-dipping flows and minor rugosity along gabbroic basement
15	100	0.50	5000.0	10.0	20000	50000	similar to case 0
16	100	0.50	2500.0	10.0	20000	12500	Similar to case 0
17	100	0.50	2500.0	10.0	20000	25000	Similar to case 0
18	100	0.50	2500.0	10.0	20000	100000	symmetric and smooth seaward-dipping flows; localized deformation along the axis divides flows into conjugate packages that rotate due to spreading and burial; total flow thickness increases away from spreading axis from 2 to 5 km; smooth and uniform gabbroic basement surface with very minor rugosity;
19	100	0.10	2500.0	10.0	20000	50000	relatively thin symmetric seaward-dipping flow packages with minor rugosity in gabbroic basement
20	100	0.20	2500.0	10.0	20000	50000	relatively thin symmetric seaward-dipping flow packages with minor rugosity in gabbroic basement
21	100	0.30	2500.0	10.0	20000	50000	moderate thickness symmetric to asymmetric seaward-dipping flow packages with minor rugosity in gabbroic basement
22	100	0.40	2500.0	10.0	20000	50000	similar to case 0 but with less total lava thickness
23	100	0.60	2500.0	10.0	20000	50000	similar to case 0 but with greater total lava thickness
24	100	0.70	2500.0	10.0	20000	50000	similar to case 0 but with greater total lava thickness
25	100	0.10	2500.0	10.0	20000	75000	similar to case 0 but with greater symmetry between seaward-dipping conjugate flows
26	100	0.30	2500.0	10.0	20000	75000	similar to case 18 but with less total lava thickness
27	100	0.50	2500.0	10.0	20000	75000	similar to case 18
28	100	0.70	2500.0	10.0	20000	75000	similar to case 18 but with greater total lava thickness
29	100	0.10	2500.0	10.0	20000	100000	similar to case 18 but with less total lava thickness (1-1.25 km)
30	100	0.20	2500.0	10.0	20000	100000	similar to case 18 but with less total lava thickness (2-2.5 km)
31	100	0.30	2500.0	10.0	20000	100000	similar to case 18 but with less total lava thickness
32	100	0.70	2500.0	10.0	20000	100000	similar to case 18 but with greater total lava thickness (5-7 km)
33	100	0.10	2500.0	1.0	20000	50000	similar to case 9 but with thinner volcanic packages and lower-amplitude gabbroic ridges
34	100	0.20	2500.0	1.0	20000	50000	similar to case 9 but with thinner volcanic packages and lower-amplitude gabbroic ridges
35	100	0.30	2500.0	1.0	20000	50000	similar to case 9 but with thinner volcanic packages and lower-amplitude gabbroic ridges
36	100	0.40	2500.0	1.0	20000	50000	similar to case 9 but with thinner volcanic packages and lower-amplitude gabbroic ridges

Table 7: Model cases and variable parameter values.

Figures

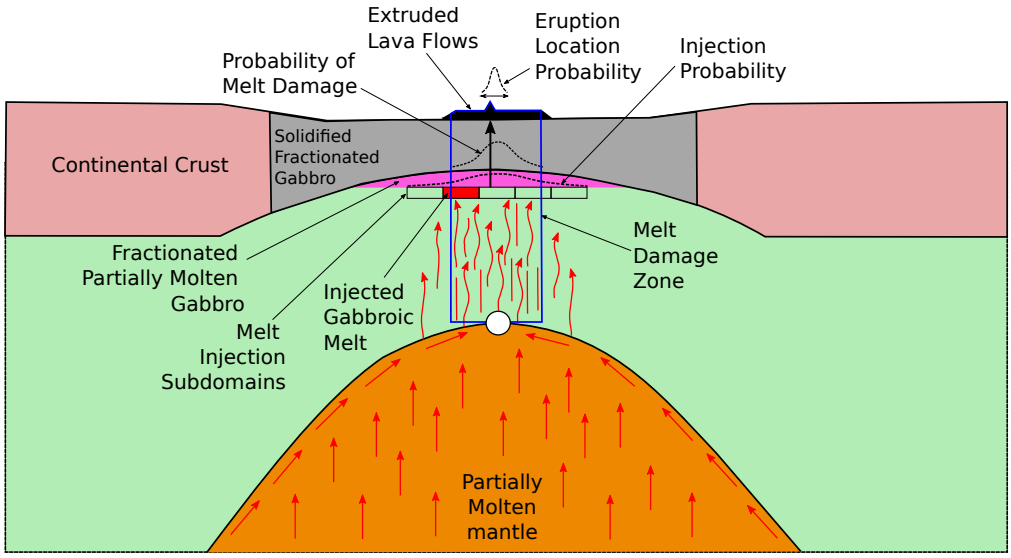

Figure 1: Schematic illustration of the melt-processes model used in this work including melt extraction, melt transport, melt emplacement, melt extrusion and melt damage. Melt is assumed to undergo instantaneous vertical migration through the partially molten asthenosphere until a permeability barrier is reached, which is assumed to be at the top of the partially molten domain. Melt then migrates along the permeability barrier toward the melt focusing point after which it is transported to the base of the Moho via channelized networks and dike injection. Melt is probabilistically injected into subdomains at the base of the Moho based on a normal probability distribution to simulate the natural variability associated with dikes and channelized networks. Melt damage is applied in in the melt-damage-zone zone by reducing the friction angle and cohesion of probabilistically selected markers to approximate the effects of channelized melt networks and dike injection on lithospheric strength. A fraction of the extracted melt is extruded onto the topographic surface of the model (thick black arrow) and allowed to laterally flow based on a cellular automata model.

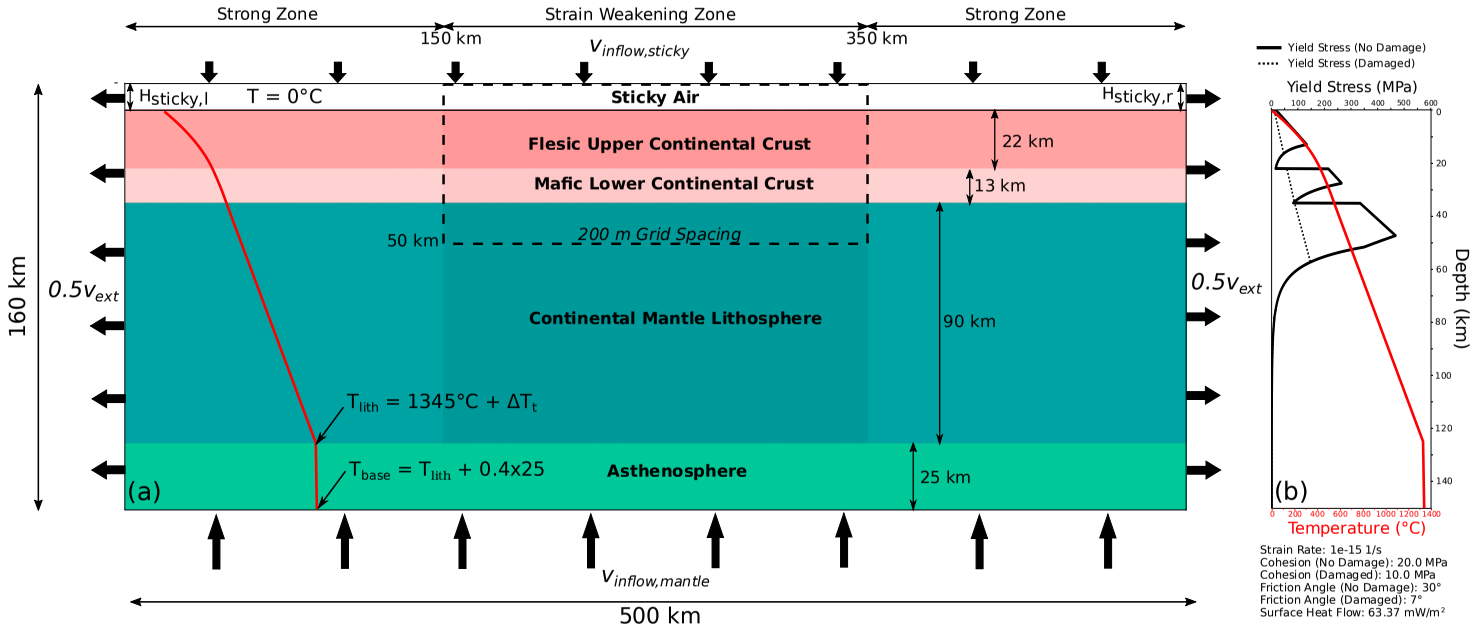

Figure 2: Model setup showing (a) the initial model geometry and boundary conditions, and (b) the initial thermal structure and yield stress profile. The model domain is 500 km by 160 km and consists of a 10 km thick sticky air layer overlying a 22 km thick felsic upper continental crust (wet quartzite rheology), a 13 km thick mafic lower continental crust (wet anorthite rheology), a 90 km thick continental mantle lithosphere (dry olivine aggregate rheology), and a 25 km thick asthenosphere layer (dry olivine aggregate rheology). Strain weakening is disabled in lateral strong zones to localize deformation in the central region of the model domain. The top boundary temperature is fixed at 0°C, while the basal temperature is initially set to $T_{base} = T_{lith} + 0.4x25$ where $T_{lith} = 1345°C + \Delta T_1$ is the temperature at the base of the continental lithosphere and ΔT_t is the thermal anomaly associated with a plume head that rapidly ascends through the asthenosphere and spreads out laterally beneath the continental lithosphere. After 1 Myr, the basal temperature is recomputed using $T_{lith} = 1345 \circ C$. The initial asthenosphere thermal structure follows an adiabatic gradient of 0.4°C/km. Velocity boundary conditions involve outflow velocities of $0.5v_{ext}$ on the side boundaries and compensating inflow velocities $v_{inflow,sticky}$ and $v_{inflow,mantle}$ on the top and bottom boundaries to maintain volume conservation. Panel (b) shows the temperature profile (red curve) and yield stress profiles for both undamaged material with a friction angle of 30° (solid black line) and damaged material with a friction angle of 7° (dashed black line). See text for additional details.

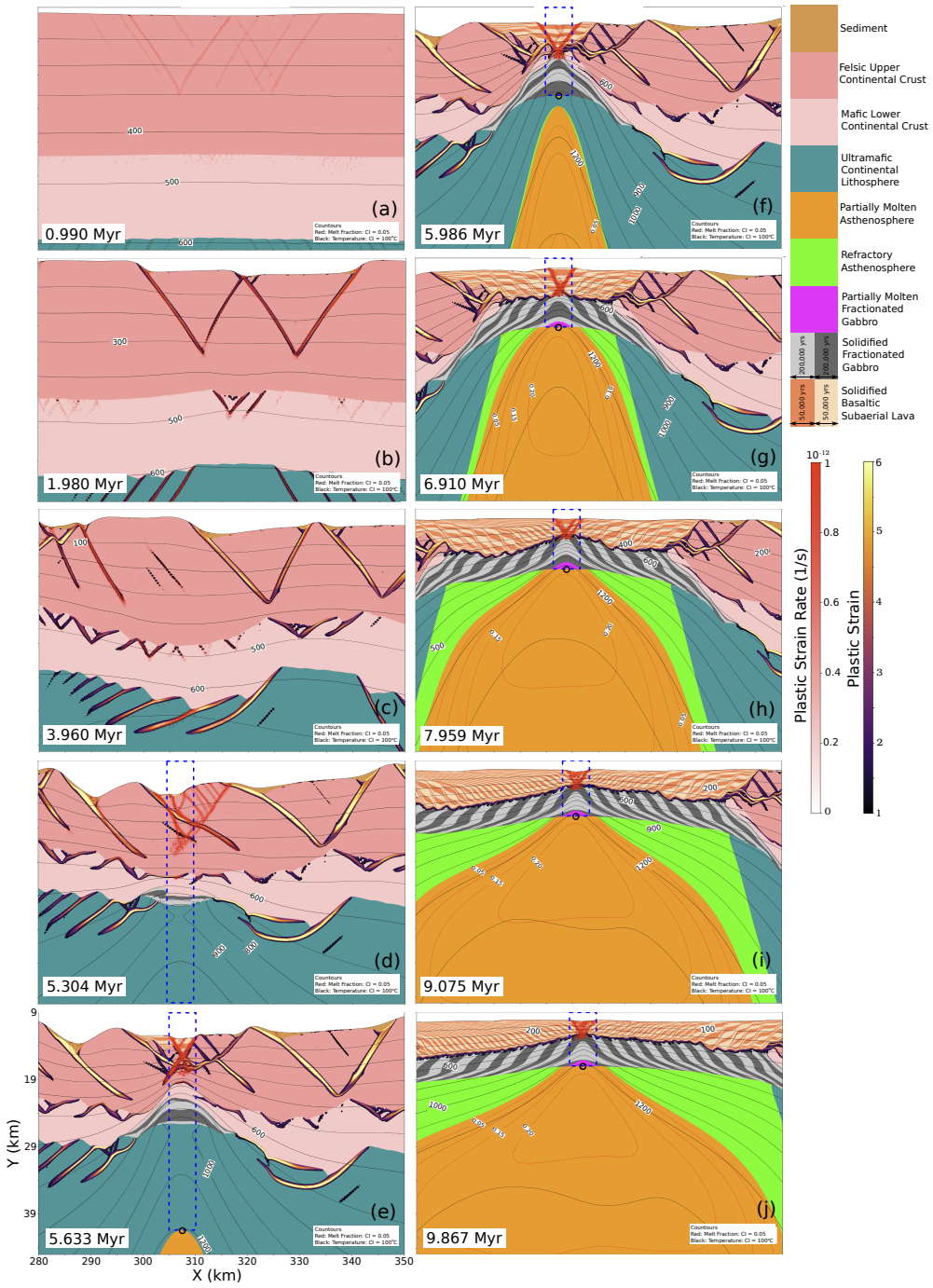

Figure 3: Base-case model (Case 0) with probabilistic melt damage and inter-eruption period of 50,000 yr. Marker composition is shown with overlays for plastic strain and plastic strain rate. Panels (a-e) show the early stages of rifting and initial gabbroic emplacement. Panels (f-j) show the later stages of magmatic crust formation and subaerial flow development. The melt-damage zone is denote with a blue dashed box. The open black circle denotes the location of the melt focusing point (i.e. shallowest point in the partially molten asthenosphere). Decompression melting generates partially molten asthenosphere (orange) which transforms to refractory asthenosphere once sufficient cooling occurs. Melt extraction produces intrusive gabbro bodies represented as dark and light bands of gray to show 200,000 yr solidification intervals. Packages of subaerial flows are represented as dark and light orange bands representing 50,000 yr intervals. See Table 7 for the model parameters and the text for additional details.

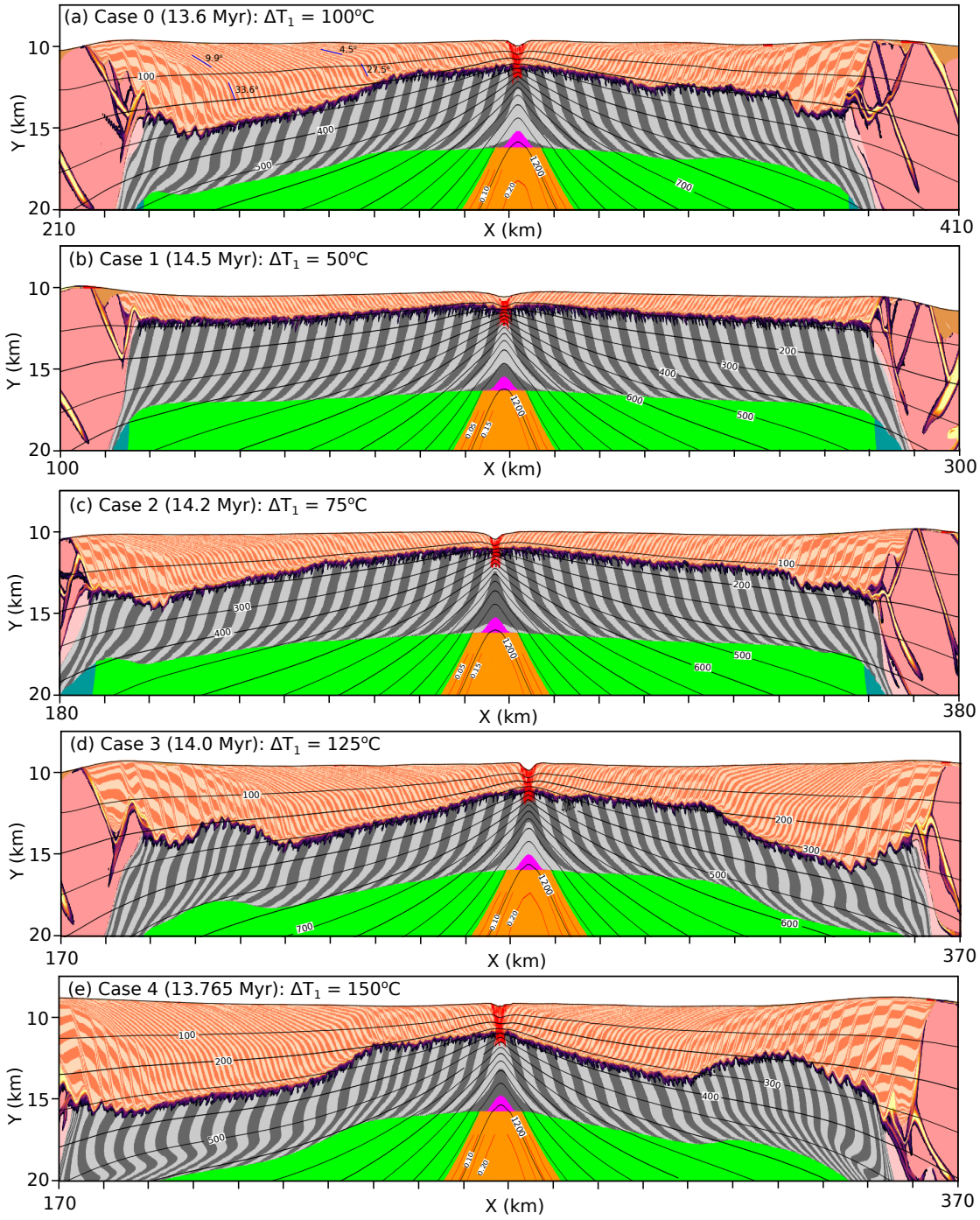

Figure 4: Effects of plume head thermal anomaly (ΔT_1) on flow geometry and magmatic crust formation (Cases 0-3). See Figure 3 for an a description of figure colors and Table 7 for the model parameters. All panels show model snapshots at approximately 13.6-14.5 Myr after the onset of extension and significant magmatic crust formation. Panels (a-e) show different cases using identical model parameters but different thermal anomalies ΔT_1. The dip of selected lava-flow packages is shown on the left-conjugate plate in (a). See the text for additional details.

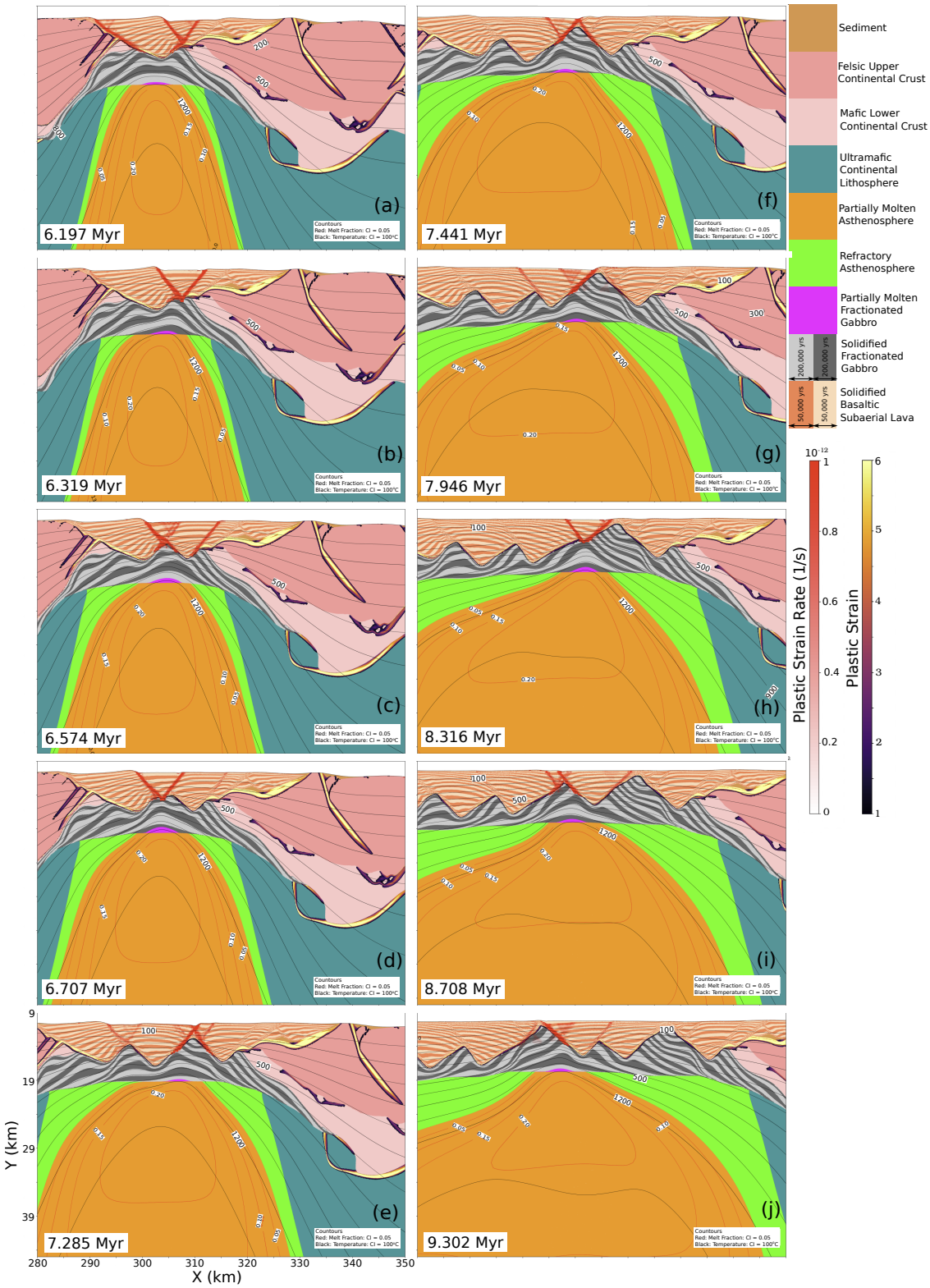

Figure 5: Panels (a-j) show magmatic crust formation without probabilistic melt damage (Case 9). See Figure 3 for an a description of figure colors and Table 7 for the model parameters.

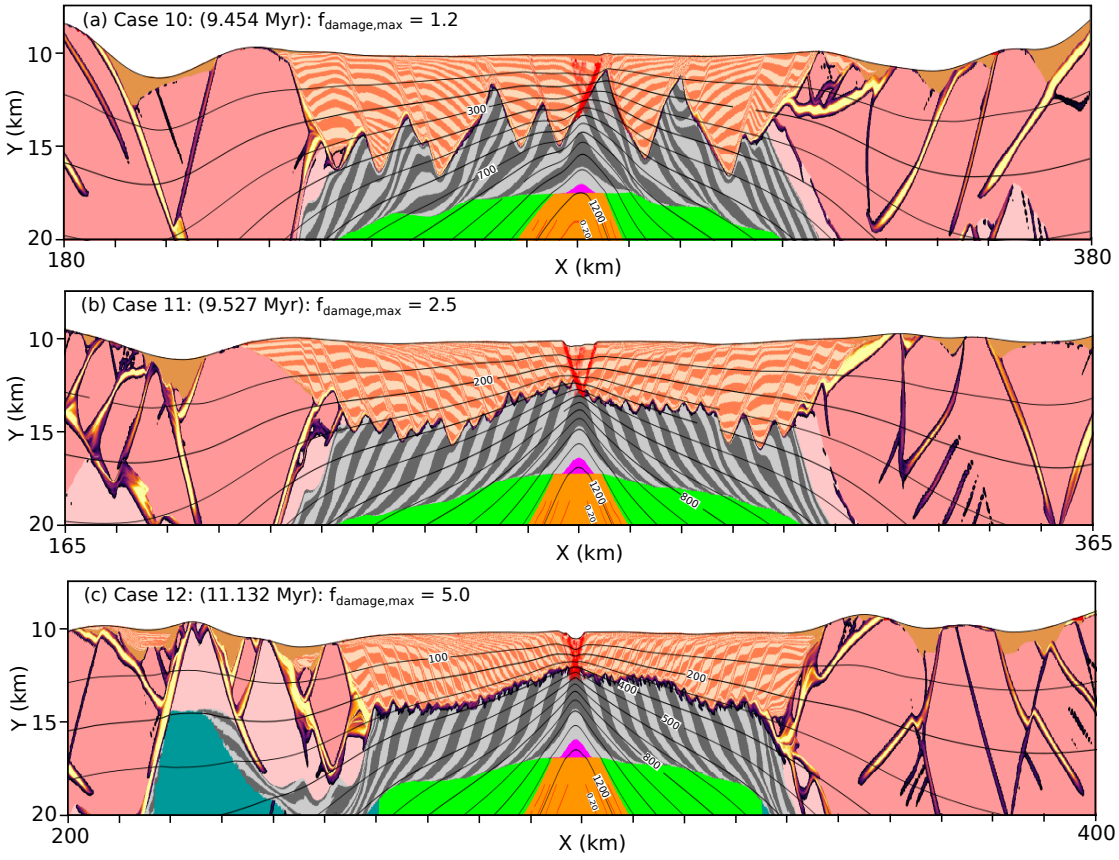

Figure 6: Effects of maximum melt damage factor (Cases 10-12). See Figure 3 for an a description of figure colors and Table 7 for the model parameters. See the text for additional details.

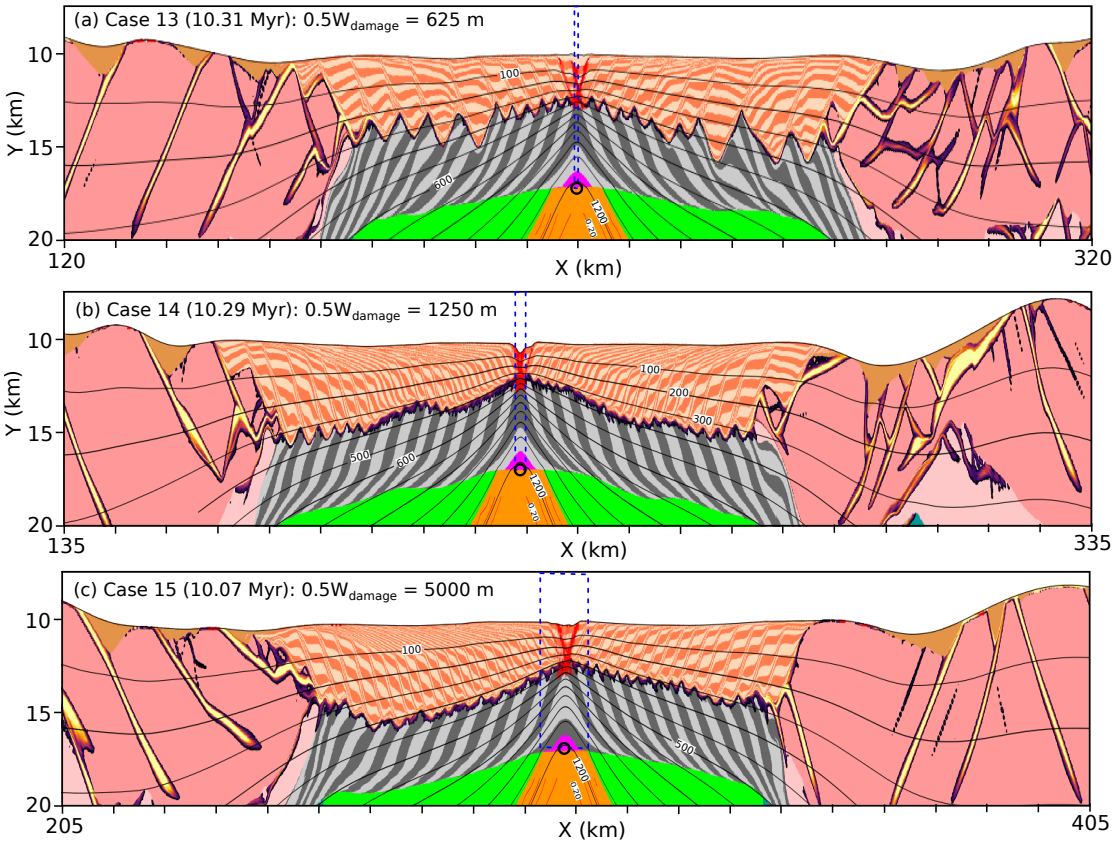

Figure 7: Effects of width of melt damage zone (Cases 13-14). See Figure 3 for an a description of figure colors and Table 7 for the model parameters. See the text for additional details.

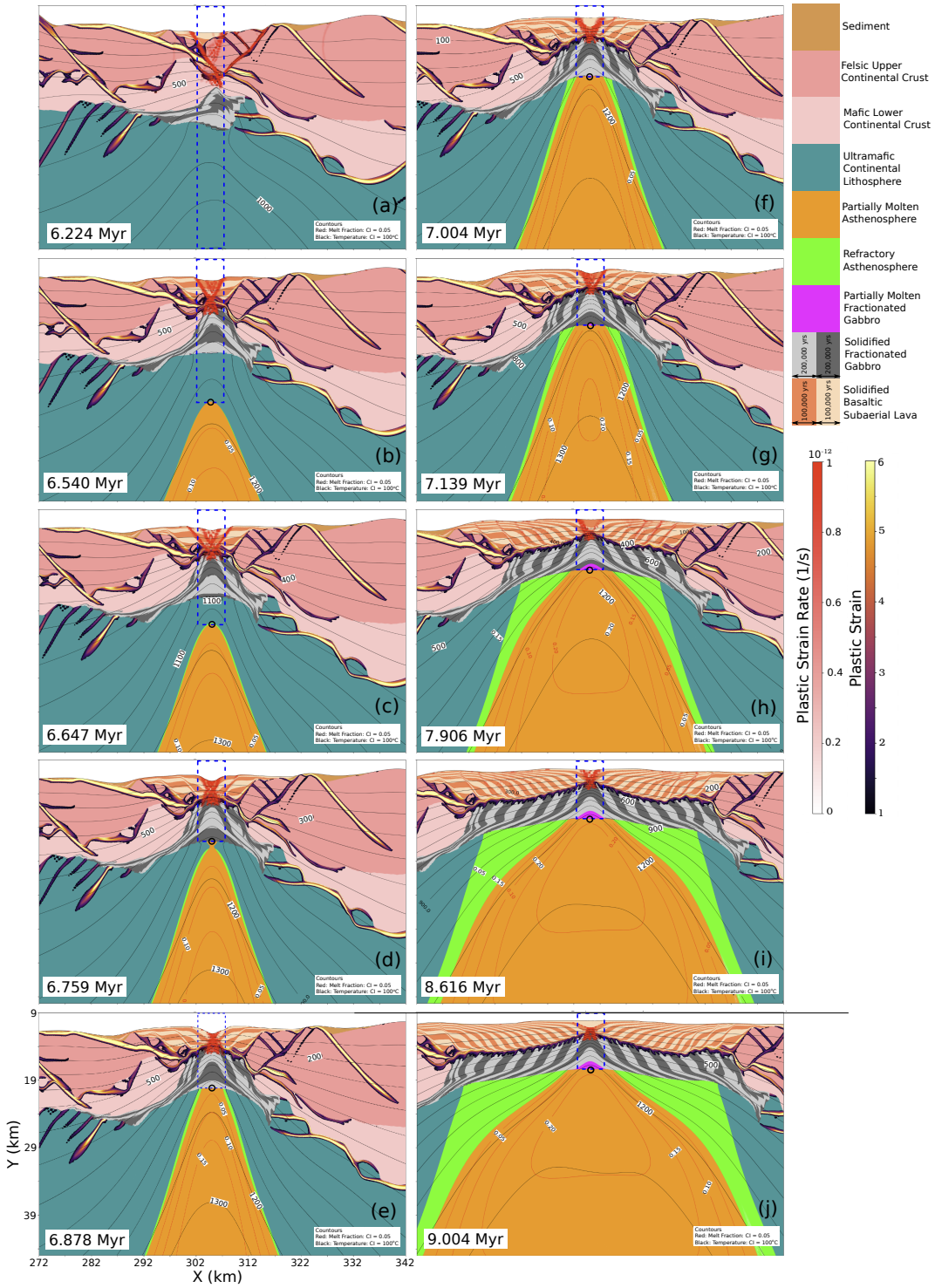

Figure 8: Magmatic crust formation with inter-eruption period of 100,000 yrs (Case 18). See Figure 3 for an a description of figure colors and Table 7 for the model parameters. See the text for additional details.

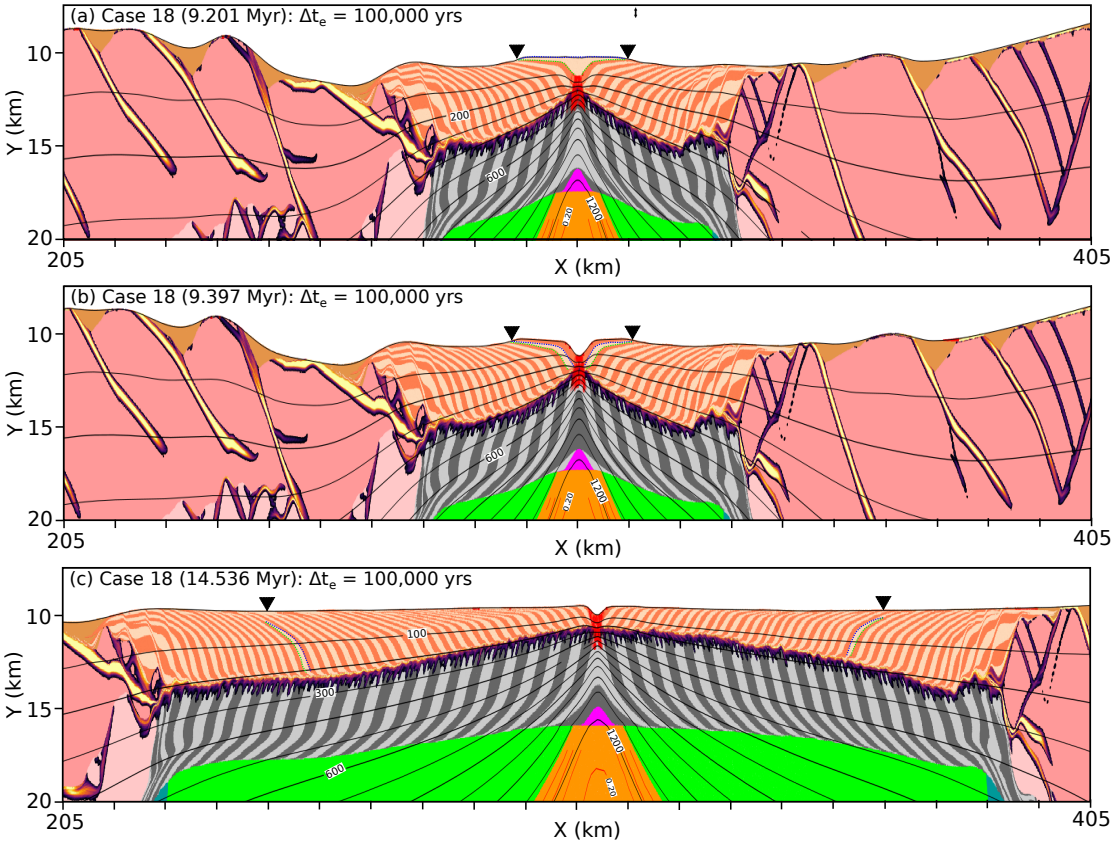

Figure 9: Closer look at magmatic crust formation with inter-eruption period of 100,000 yrs (Case 18). See Figure 3 for an a description of figure colors and Table 7 for the model parameters. See the text for additional details.

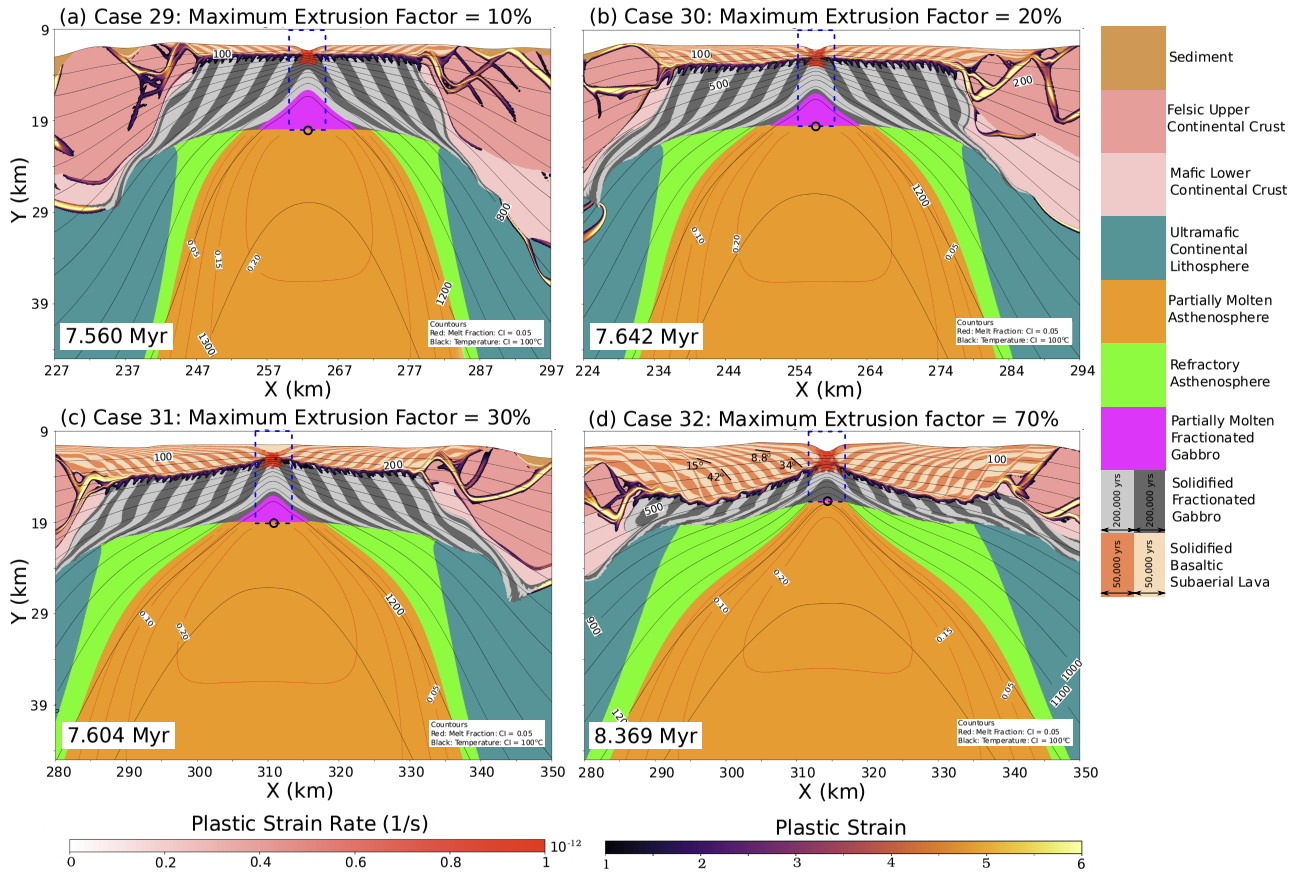

imum extrusion factor (Cases 29-30). See Figure 3 for an a description of figure colors and Table 7 for the model parameters. The dip of selected lava-flow packages is shown on the left-conjugate plate in (d). See the

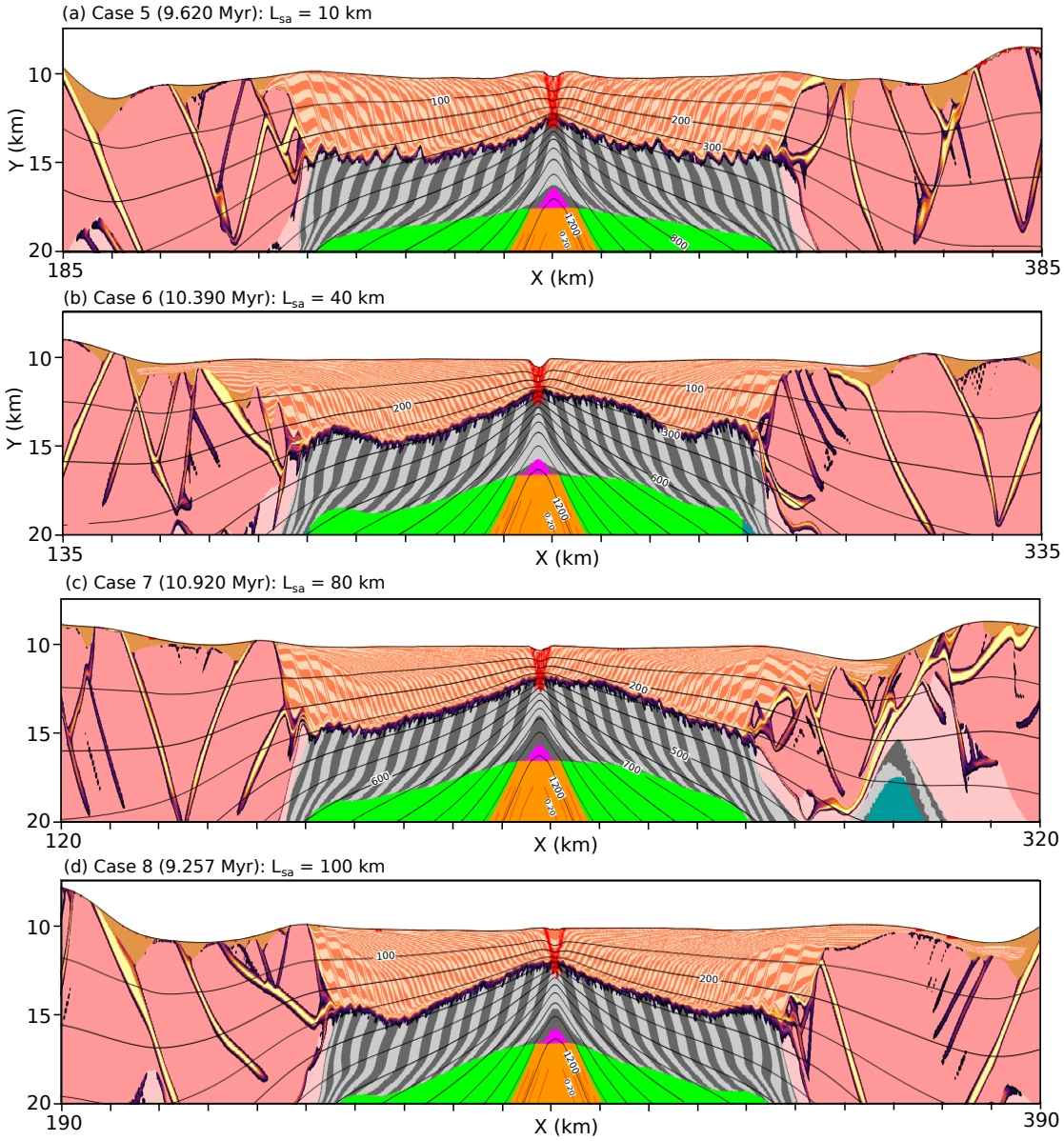

Figure 11: Effects of the characteristic length of subaerial flows (Cases 5-8). See Figure 3 for an a description of figure colors and Table 7 for the model parameters. See the text for additional details.

Appendix

Appendix A. Algorithm for Solving the Visco-elasto-plastic Stokes-Continuity Equations

The frictional-plastic failure model used in this work introduces a strong non-linearity where the visco-plastic viscosity $\eta_{vp,m}$ is dependent on deviatoric stress and deviatoric stress is in turn dependent on the visco-plastic viscosity as described in equations (9) and (10). This work uses the Picard iteration method to iteratively solve the non-linear Stokes-continuity equations on the staggered grid. The deviatoric stress tensor is updated on markers that are advected with the velocity field. Updating the deviatoric stress tensor components on markers requires accounting for stress changes from three sources:

1. deviatoric grid stress changes from equation obtained on the Eulerian staggered grid by solving the non-linear Stokes-continuity equation with visco-elasto-plastic stress forecast,

2. deviatoric stress changes occurring at a subgrid scale on individual markers,

3. deviatoric stress changes associated with the rotation of markers during advection.

The following algorithm is used to solve equations (1), (2), and (7) using the visco-elasto-plastic constitutive law described in equations (4) and (5), and to update the deviatoric stress tensor components on markers for the three sources of stress changes.

For each time step t do:

1. Set model time step Δt equal to visco-elastic time step Δt_{ve}.

2. Calculate deviatoric stress components $\sigma'_{xx(i,j)_{p1}}$ and $\sigma'_{xy(i,j)_{b1}}$ and visco-plastic viscosity $\eta_{vp(i,j)_p}$ and $\eta_{vp(i,j)_b}$ on staggered grid by interpolating marker deviatoric stress components $\sigma'_{xx,m}$ and $\sigma'_{xy,m}$ and marker visco-plastic viscosity $\eta_{vp,m}$ using equation (C.1). The subscripts p and b refer to the pressure and basic grids, respectively.

3. Run the Picard iteration loop (section Appendix A.0.1) to obtain new solutions for the x-component of velocity $v_{x(i,j)_{vx}}$, the y-component of velocity $v_{y(i,j)_{vy}}$ and pressure $P_{(i,j)_p}$. The subscripts v_x and v_y refer to the x-velocity and y-velocity staggered grids, respectively [21, 20].

4. Interpolate visco-plastic viscosity from basic grid $\eta_{vp(i,j)_b}$ to markers using a harmonic average (section Appendix A.0.3).

5. Update model time step Δt ensuring that displacement is less than 30% of the staggered grid spacing based on current velocity solutions $v_{x(i,j)_{vx}}$ and $v_{y(i,j)_{vy}}$ and grid spacings $\Delta x_{(i,j)_{vx}}$ and $\Delta y_{(i,j)_{vy}}$.

6. Forecast deviatoric stresses $\sigma'_{xx(i,j)_{p2}}$ and $\sigma'_{xy(i,j)_{b2}}$ using equation (A.7) with updated deviatoric strain rates $\dot{\epsilon}'_{xx(i,j)_p}$ and $\dot{\epsilon}'_{xy(i,j)_b}$, updated visco-plastic viscosity $\eta_{vp(i,j)_p}$ and $\eta_{vp(i,j)_b}$ and updated model time step Δt.

7. Update grid deviatoric stress changes using the following equations:

$$\begin{aligned} \Delta\sigma'_{xx(i,j)_p} &= \sigma'_{xx(i,j)_{p2}} - \sigma'_{xx(i,j)_{p1}} \\ \Delta\sigma'_{xy(i,j)_b} &= \sigma'_{xy(i,j)_{b2}} - \sigma'_{xy(i,j)_{b1}} \end{aligned} \tag{A.1}$$

8. Update marker deviatoric stress components $\sigma'_{xx,m}$ and $\sigma'_{xy,m}$ for subgrid changes using subgrid stress diffusion (section Appendix A.0.4).

9. Advect markers and calculate marker angular velocity ω_m using the 4-th order Runge-Kutta method and angular velocity on the basic grid $\omega_{(i,j)_b}$ given by:

$$\omega_{(i,j)_b} = 0.5\left(\frac{\left(v_{y(i,j+1)vy} - v_{y(i,j)vy}\right)}{\Delta x_{vy(j)}} - \frac{\left(v_{x(i+1,j)vx} - v_{x(i,j)vx}\right)}{\Delta y_{vx(i)}}\right) \tag{A.2}$$

10. Update marker deviatoric stress components $\sigma'_{xx,m}$ and $\sigma'_{xy,m}$ for rotation using the following equations:

$$\begin{aligned} \sigma'_{xx,m} = \sigma'^{o}_{xx,m}\left(\cos(\omega_m\Delta t)^2 - \sin(\omega_m\Delta t)^2\right) - \sigma'^{o}_{xy,m}\sin(2\omega_m\Delta t), \\ \sigma'_{xy,m} = \sigma'^{o}_{xx,m}\sin(2\omega_m\Delta t) + \sigma'^{o}_{xy,m}\cos(2\omega_m\Delta t) \end{aligned} \tag{A.3}$$

where $\sigma'^{o}_{xx,m}$ and $\sigma'^{o}_{xy,m}$ are the deviatoric marker stress components before advection.

11. Advance model time t by Δt.

End time step loop

Appendix A.0.1. Picard Iteration Loop

While Picard criterion $R_{L2} > Tolerance$ **and** $N_{iterations} < N_{max}$ **do:**

(1) Calculate the visco-plastic viscosity on pressure grid $\eta_{vp(i,j)_p}$ as a harmonic average of the visco-plastic viscosity $\eta_{vp(i,j)_b}$ on surrounding basic nodes:

$$\eta_{vp(i,j)_p} = \frac{4}{1/\eta_{vp(i,j)_b} + 1/\eta_{vp(i-1,j)_b} + 1/\eta_{vp(i,j-1)_b} + 1/\eta_{vp(i-1,j-1)_b}} \tag{A.4}$$

(2) Obtain new solution vector S^{new} and updated solutions for x-component of velocity $v_{x(i,j)_{vx}}$, y-component of velocity $v_{y(i,j)_{vy}}$ and pressure $P_{(i,j)_p}$ by solving equations (1), (2), and (7) using current $\eta_{vp(i,j)_b}$ and $\eta_{vp(i,j)_p}$.

(3) Update the convergence criterion R_{L2}defined as:

$$R_{L2} = \frac{\sqrt{\sum_i (S^{new}_{v_{xy},i} - S^{old}_{v_{xy},i})^2}}{\sqrt{\sum_i (S^{new}_{v_{xy},i})^2}} \tag{A.5}$$

where $S^{old}_{v_{xy}}$ is the old velocity solution vector and $S^{new}_{v_{xy}}$ is the new velocity solution vector.

(4) Calculate deviatoric strain rate components $\dot{\epsilon}'_{xx(i,j)_p}$ and $\dot{\epsilon}'_{xy(i,j)_b}$ using updated velocity solutions $v_{x(i,j)vx}$ and $v_{y(i,j)vy}$ and the following equation:

$$\dot{\epsilon}'_{xx(i,j)_p} = \frac{1}{2}\left(\frac{v_{x(i+1,j+1)vx} - v_{x(i+1,j)vx}}{\Delta x_{j_b}} - \frac{v_{y(i+1,j+1)vy} - v_{y(i,j+1)vy}}{\Delta y_{i_b}}\right) \quad \text{and}$$
$$\dot{\epsilon}'_{xy(i,j)_b} = \frac{1}{2}\left(\frac{v_{x(i+1,j)vx} - v_{x(i,j)vx}}{\Delta y_{i_p}} + \frac{v_{y(i,j+1)vx} - v_{y(i,j)vx}}{\Delta x_{j_p}}\right), \tag{A.6}$$

(5) Forecast deviatoric stresses $\sigma'_{xx(i,j)_{p2}}$ and $\sigma'_{xy(i,j)_{b2}}$ using updated deviatoric strain rates $\dot{\epsilon}'_{xx(i,j)_p}$ and $\dot{\epsilon}'_{xy(i,j)_b}$, updated visco-plastic viscosity $\eta_{vp(i,j)_p}$ and $\eta_{vp(i,j)_b}$ with the following equations:

$$\begin{aligned}
\sigma'_{xx(i,j)_{p2}} &= 2\eta_{vp(i,j)_p}\dot{\epsilon}'_{xx(i,j)_p}\frac{\mu_{(i,j)_b}\Delta t}{\mu_{(i,j)_b}\Delta t + \eta_{vp(i,j)_p}} \\
&\quad + \sigma'_{xx(i,j)_{p1}}\frac{\eta_{vp(i,j)_p}}{\mu_{(i,j)_b}\Delta t + \eta_{vp(i,j)_p}} \\
\sigma'_{xy(i,j)_{b2}} &= 2\eta_{vp(i,j)_b}\dot{\epsilon}'_{xy(i,j)_b}\frac{\mu_{(i,j)_b}\Delta t}{\mu_{(i,j)_b}\Delta t + \eta_{vp(i,j)_b}} \\
&\quad + \sigma'_{xy(i,j)_{b1}}\frac{\eta_{vp(i,j)_b}}{\mu_{(i,j)_b}\Delta t + \eta_{vp(i,j)_b}}
\end{aligned} \tag{A.7}$$

(6) Update visco-plastic viscosity $\eta_{vp(i,j)_b}$ for yielding and plastic failure flag $\chi_{(i,j)_b}$ on basic grid (section Appendix A.0.2).

End Picard iteration loop

It was observed that the node-based plasticity scheme stable convergence compared to marker based methods, an observation consistent with the work of [22]. Furthermore, for the cases tested in this study, convergence criteria could be achieved if the model time step was sufficiently small. For the models presented in this work $R_{L2} = 10^{-4}$ was used as the Picard convergence criterion.

Appendix A.0.2. Nodal Plasticity Update
For each basic node (i, j) **do:**

(1) Calculate the second invariant of deviatoric stress $\sigma'_{II(i,j)_b}$ using equation updated deviatoric stresses $\sigma'_{xx(i,j)_{b2}}$ and $\sigma'_{xy(i,j)_{b2}}$ and the following equation:

$$\sigma'_{xx,avg(i,j)_{b2}} = \frac{1}{4}\left(\sigma'_{xx(i,j)_{p2}} + \sigma'_{xx(i+1,j)_{p2}} + \sigma'_{xx(i,j+1)_{p2}} + \sigma'_{xx(i+1,j+1)_{p2}}\right),$$
$$\sigma'_{II(i,j)_b} = \sqrt{\left(\left(\sigma'_{xy(i,j)_{b2}}\right)^2 + \left(\sigma'_{xx,avg(i,j)_{b2}}\right)^2\right)} \tag{A.8}$$

(2) Compute the second invariant of deviatoric stress for purely elastic stress buildup $\sigma'_{II,elastic(i,j)_b}$ using the following equation:

$$\sigma'_{II,elastic(i,j)_b} = \frac{\mu_{(i,j)_b}\Delta t + \eta_{vp(i,j)_b}}{\eta_{vp(i,j)_b}}\sigma'_{II(i,j)_b} \tag{A.9}$$

where $\mu_{(i,j)_b}$ is the shear modulus at basic nodes and Δt is the model time step.

(3) Interpolate pressure from staggered pressure grid $P_{(i,j)_p}$ to basic pressure grid $P_{(i,j)_b}$:

$$P_{(i,j)_b} = \frac{1}{4}\left(P_{(i,j)_p} + P_{(i+1,j)p} + P_{(i,j+1)p} + P_{(i+1,j+1)p}\right) \tag{A.10}$$

(4) Compute the Drucker-Prager yield stress on basic grid $\sigma_{\text{yield}(i,j)_b}$ using the following equation:

$$\sigma_{yield(i,j)} = \begin{cases} \sigma_{c(i,j)_b}\cos(\theta_{(i,j)_b}) & \\ \quad + \sin(\theta_{(i,j)_b})\left(P_{(i,j)_b} - P_f\right) & \text{for } P_{(i,j)_b} \geq P_f \\ \sigma_{c(i,j)_b}\cos(\theta_{(i,j)_b}) & \text{for } P_{(i,j)_b} < P_f \end{cases} \tag{A.11}$$

where $\sigma_{yield(i,j)}$ is the second invariant of the deviatoric stress tensor at basic grid node at yield, $\sigma_{c(i,j)_b}$ is the cohesion, $\theta_{(i,j)_b}$ is the friction angle and and P_f is the fluid pressure.

(5) Update visco-plastic viscosity $\eta_{vp(i,j)_b}$ for plastic failure using the following equation:

$$\eta_{vp(i,j)_b} = \begin{cases} \eta_{creep(i,j)_b} & \text{for} \quad \sigma'_{II,elastic(i,j)_b} \leq \sigma_{yield(i,j)_b} \\ \min\left(\eta_{yield(i,j)_b}, \eta_{creep(i,j)_b}\right) & \text{for} \quad \sigma'_{II,elastic(i,j)_b} > \sigma_{yield(i,j)_b} \end{cases} \tag{A.12}$$

where $\eta_{creep(i,j)_b}$ is the composite creep viscosity calculated on markers using equation (83) and $\eta_{yield(i,j)_b}$ is the visco-plastic viscosity at the yield state as given by:

$$\eta_{yield(i,j)_b} = \mu_{(i,j)_b} \Delta t \frac{\sigma_{yield(i,j)_b}}{\sigma'_{II,elastic(i,j)_b} - \sigma_{yield(i,j)_b}} \tag{A.13}$$

(6) Update the plastic yielding state on basic nodes $\chi_{(i,j)_b}$ using the following equation:

$$\chi_{(i,j)_b} = \begin{cases} 1 & \text{if } \sigma'_{II,elastic(i,j)_b} > \sigma_{yield(i,j)_b} \text{ and } \eta_{yield(i,j)_b} < \eta_{creep(i,j)_b} \\ 0 & \text{otherwise} \end{cases} \tag{A.14}$$

where a value of 1 indicates that the basic node has undergone plastic failure and a value of 0 indicates that the basic node has not undergone plastic failure.

End basic node loop

Appendix A.0.3. Harmonic Viscosity Average for Yielding
For each marker m **do:**

(1) Determine if plastic yielding has occurred for any basic node associated with the cell that contains marker m using the plastic failure criterion $\chi_{(i,j)_b}$ defined on the basic grid.

(2) Initialize the visco-plastic viscosity of the marker $\eta_{vp,m}$ to the creep viscosity $\eta_{creep(m)}$.

(3) If plastic yielding has occurred on a node associated with marker m calculate the visco-plastic viscosity of the marker $\eta_{vp,m}$ using a harmonic average limited by the flow viscosity $\eta_{creep,m}$ as follows:

$$\eta_{yield,m} = \left(\chi_{(UL)_b} w_{UL,m} + \chi_{(LL)_b} w_{LL,m} + \chi_{(UR)_b} w_{UR,m} + \chi_{(LR)_b} w_{LR,m}\right) \left(\frac{\chi_{(UL)_b} w_{UL,m}}{\eta_{vp(UL)_b}} + \frac{\chi_{(LL)_b} w_{LL,m}}{\eta_{vp(LL)_b}} + \frac{\chi_{(UR)_b} w_{UR,m}}{\eta_{vp(UR)_b}} + \frac{\chi_{(LR)_b} w_{LR,m}}{\eta_{vp(LR)_b}}\right)^{-1},$$
$$\eta_{vp,m} = \min\left(\eta_{yield,m},\, \eta_{creep,m}\right) \tag{A.15}$$

where $UL = (i_{ul,m}, j_{ul,m})$, $LL = (i_{ul,m}+1, j_{ul,m})$, $UR = (i_{ul,m}, j_{ul,m}+1)$, and $LR = (i_{ul,m}+1, j_{ul,m}+1)$ are the basic nodes indices associated with the cell containing marker m and $w_{UL,m}$, $w_{LL,m}$, $w_{UR,m}$, and $w_{LR,m}$ are the associated node-marker weights calculated using equation (C.3) and $i_{ul,m}$ and $j_{ul,m}$ are the indices of the upper-left basic grid node of the cell containing marker m.

End marker loop

Appendix A.0.4. Subgrid Stress Diffusion Steps

(1) Calculate initial nodal stresses $\sigma'_{xx,nodal,m}$ and $\sigma'_{xy,nodal,m}$ for each marker m by interpolating $\sigma'_{xx(i,j)_{p1}}$ and $\sigma'_{xy(i,j)_{b1}}$ to markers using equation (C.2).

(2) Calculated the total subgrid stress differences $\Delta\sigma'_{xx,sgt,m}$ and $\Delta\sigma'_{xy,sgt,m}$ for each marker m using the following equations:

$$\begin{aligned} \Delta\sigma'_{xx,sgt,m} &= \sigma'_{xx,nodal,m} - \sigma'_{xx,m} \\ \Delta\sigma'_{xy,sgt,m} &= \sigma'_{xy,nodal,m} - \sigma'_{xy,m}. \end{aligned} \tag{A.16}$$

(3) Calculate the relaxed subgrid stress differences $\Delta\sigma'_{xx,sg,m}$ and $\Delta\sigma'_{xy,sg,m}$ using the following equations:

$$\begin{aligned} \Delta\sigma'_{xx,sg,m} &= \Delta\sigma'_{xx,sgt,m}\left(1 - \exp\left(-D_{sg}\frac{\Delta t}{t_{max}}\right)\right) \\ \Delta\sigma'_{xy,sg,m} &= \Delta\sigma'_{xy,sgt,m}\left(1 - \exp\left(-D_{sg}\frac{\Delta t}{t_{max}}\right)\right) \end{aligned} \tag{A.17}$$

where D_{sg} is the sub-grid diffusion coefficient and t_{max} is the Maxwell time defined as:

$$t_{max} = \frac{\eta_{vp,m}}{\mu_m}. \tag{A.18}$$

(4) Calculate the relaxed sub-grid stress differences on the staggered grids $\Delta\sigma'_{xx,sg(i,j)_p}$ and $\Delta\sigma'_{xy,sg(i,j)_b}$ by interpolating the relaxed subgrid stress differences from markers $\Delta\sigma'_{xx,sg,m}$ and $\Delta\sigma'_{xy,sg,m}$ to the staggered grid using the bilinear interpolation method described in equation (C.1).

(5) Calculate the remaining stress changes on staggered grid nodes by removing the interpolated relaxed sub-grid stress differences using the following equations:

$$\begin{aligned} \Delta\sigma'_{xx,vepr(i,j)_p} &= \Delta\sigma'_{xx(i,j)_p} - \Delta\sigma'_{xx,sg(i,j)_p}, \\ \Delta\sigma'_{xy,vepr(i,j)_b} &= \Delta\sigma'_{xy(i,j)_b} - \Delta\sigma'_{xy,sg(i,j)_b} \end{aligned} \tag{A.19}$$

(6) Calculate the remaining visco-elasto plastic stress changes $\Delta\sigma'_{xx,vepr,m}$ and $\Delta\sigma'_{xy,vepr,m}$ for each marker m by interpolating the remaining stress changes on staggered grid nodes $\Delta\sigma'_{xx,vepr(i,j)_b}$ and $\Delta\sigma'_{xy,vepr(i,j)_b}$ to markers using equation (C.2).

(7) Update marker deviatoric stress components $\sigma'_{xx,m}$ and $\sigma'_{xx,m}$ using the following equations:

$$\begin{aligned} \sigma'_{xx,m} &= \sigma'^{o}_{xx,m} + \Delta\sigma'_{xx,sg,m} + \Delta\sigma'_{xx,vepr,m,}, \\ \sigma'_{xy,m} &= \sigma'^{o}_{xy,m} + \Delta\sigma'_{xy,sg,m} + \Delta\sigma'_{xy,vepr,m} \end{aligned} \tag{A.20}$$

where $\sigma'^{o}_{xx,m}$ and $\sigma'^{o}_{xy,m}$ are the previous marker deviatoric stress components.

Appendix B. Algorithm for Solving the Heat Advection-Diffusion Equation

The Eulerian-Lagrangian marker-in-cell approach from [21] is used to solve equation (17) whereby markers are advected using a 4th-order Runge-Kutta scheme and marker temperature T_m is updated using the conductive temperature solution on Eulerian grid nodes and temperature changes associated with subgrid thermal diffusion as described in the following steps:

For each time step do:

1. Interpolate current marker temperature T_m to basic grid nodes $T_{(i,j)_b}$ using equation (C.1).
2. Calculate purely conductive temperature solution over time interval Δt on basic grid $T_{solu(i,j)_b}$ by solving equation (17) without advective terms and using current grid temperature $T_{(i,j)_b}$ as the initial condition. An adaptive time-stepping scheme is applied whereby the time step is reduced if the change in temperature exceeds a threshold of 70°C.
3. Calculate the conductive temperature change on the Eulerian grid using the following equation:

$$\Delta T_{(i,j)_b} = T_{solu(i,j)_b} - T_{(i,j)_b} \tag{B.1}$$

4. Update marker temperature T_m for subgrid temperature changes using subgrid thermal diffusion (section Appendix B.0.1).
5. Advect markers using a 4th-order Runge-Kutta scheme.
6. Advance model time t by Δt.

End time step loop

Appendix B.0.1. Subgrid Thermal Diffusion Steps

(1) Calculate the initial nodal temperature on markers $T_{nodal,m}$ by interpolating $T_{(i,j)_b}$ back to markers using equation (C.2).

(2) Calculate the total sub-grid temperature difference between interpolated nodal temperatures and current marker temperatures using the following equation:

$$\Delta T_{sgt,m} = T_{nodal,m} - T_m \tag{B.2}$$

(3) Calculate the relaxed sub-grid temperature difference on markers using the following equation:

$$\Delta T_{sg,m} = \Delta T_{sgt,m} \left(1 - \exp\left(-D_{sg} \frac{\Delta t}{t_{sg,m}}\right)\right) \tag{B.3}$$

where D_{sg} is the sub-grid diffusion coefficient, Δt is the time step and t_{sg} is the thermal diffusion time scale given by:

$$t_{sg,m} = \frac{\rho_m C_{p,m}}{k_m \left(\frac{2}{\Delta x^2} + \frac{2}{\Delta y^2}\right)} \tag{B.4}$$

where ρ_m is the density of the marker, $C_{p,m}$ is the specific heat capacity of the marker, k_m is the thermal conductivity of the marker, Δx and Δy are the grid spacings in the x and y directions, respectively.

(4) Calculate the relaxed sub-grid temperature difference on Eulerian grid $\Delta T_{sg(i,j)_b}$ by interpolating $\Delta T_{sg,m}$ using equation (C.1).

(5) Calculate the remaining temperature change $\Delta T_{r(i,j)_b}$ on Eulerian nodes by removing the relaxed sub-grid temperature difference using the following equation:

$$\Delta T_{r(i,j)_b} = \Delta T_{(i,j)_b} - \Delta T_{sg(i,j)} \tag{B.5}$$

(6) Interpolate $\Delta T_{r(i,j)_b}$ to markers using equation (C.2) to obtain $\Delta T_{r,m}$, which is the nodal temperature change with sub-grid effects removed.

(7) Update marker temperature T_m taking into account both sub-grid effects and the remaining temperature change from the basic grid using the following equation:

$$T_m = T_m + \Delta T_{sg,m} + \Delta T_{r,m} \tag{B.6}$$

Appendix C. Marker-grid Interpolation

Marker-in-cell methods require tensor and scalar parameters to be interpolated back and forth between the Eulerian grid and the Lagrangian markers. We use the first-order bilinear interpolation scheme similar to [21] for interpolating marker information to Eulerian grid nodes:

$$S_{i,j} = \frac{\sum_m S_m w_{m(i,j)}}{\sum_m w_{m(i,j)}}, \quad w_{m(i,j)} = \left(1 - \frac{\Delta x_m}{\Delta x}\right)\left(1 - \frac{\Delta y_m}{\Delta y}\right) \tag{C.1}$$

where $S(i,j)$ is the interpolated parameter value at the Eulerian grid node (i,j), S_m is the parameter value at the marker m located within one of four surrounding grid cells, $w_{m(i,j)}$ is the weight of the marker m at the Eulerian grid node (i,j), Δx_m and Δy_m are the distances between the marker m and the Eulerian grid node (i,j) in the x and y directions, respectively, and Δx and Δy are the grid spacings in the x and y directions, respectively. With our modeling approach the index i corresponds to the vertical y-axis that increases with depth and the index j corresponds to the x-axis. Two types of interpolation are used based on the size of the search radius used in (C.1): (1) inclusive interpolation

where markers within the search radius equal to Δx and Δy are used in the interpolation, and (2) exclusive interpolation where markers within the search radius equal to $0.5\Delta x$ and $0.5\Delta y$ are used in the interpolation.

A similar first-order bilinear scheme is used for interpolating parameter values from Eulerian grid nodes to Lagrangian markers:

$$\begin{aligned} S_m = S_{(i_{ul,m},j_{ul,m})} w_{UL,m} + S_{(i_{ul,m},j_{ul,m}+1)} w_{UR} \\ + S_{(i_{ul,m}+1,j_{ul,m})} w_{LL} + S_{(i_{ul,m}+1,j_{ul,m}+1)} w_{LR} \end{aligned} \tag{C.2}$$

where S_m is the interpolated parameter value at the Lagrangian marker m, $i_{ul,m}$ is the y-index of the upper left grid node for marker m, $j_{ul,m}$ is the x-index of the upper-left grid node for marker m, $S_{i_{ul,m},j_{ul,m}}$, $S_{i_{ul,m},j_{ul,m}+1}$, $S_{i_{ul,m}+1,j}$, and $S_{i_{ul,m}+1,j_{ul,m}+1}$ are the parameter values at the four surrounding Eulerian grid nodes, and $w_{UL,m}$, $w_{LL,m}$, $w_{UR,m}$, and $w_{LR,m}$ are the weights for the upper-left, lower-left, upper-right, and lower-right grid nodes, respectively. The weights of the four surrounding Eulerian grid nodes for marker m are calculated using the following equations:

$$\begin{aligned} w_{UL,m} &= (1.0 - \Delta x'_{UL})(1.0 - \Delta y'_{UL}) \\ w_{LL,m} &= (1.0 - \Delta x'_{UL})\Delta y'_{UL} \\ w_{UR,m} &= \Delta x'_{UL}(1.0 - \Delta y'_{UL}) \\ w_{LR,m} &= \Delta x'_{UL}\Delta y'_{UL} \end{aligned} \tag{C.3}$$

where $\Delta x'_{UL}$ and $\Delta y'_{UL}$ are the normalized distances in the x and y directions, respectively, between the marker and the upper-left node of the cell containing the marker as defined by the following equations:

$$\begin{aligned} \Delta x'_{UL} &= \frac{(x_m - x_{b,j_{ul,m}})}{\Delta x_{b,j_{ul,m}}} \\ \Delta y'_{UL} &= \frac{(y_m - y_{b,i_{ul,m}})}{\Delta y_{b,i_{ul,m}}} \end{aligned} \tag{C.4}$$

where x_m and y_m are the coordinates of the marker m, $x_{b,j_{ul,m}}$ and $y_{b,i_{ul,m}}$ are the coordinates of the upper-left basic grid node of the cell containing the marker m, and $\Delta x_{b,j_{ul,m}}$ and $\Delta y_{b,i_{ul,m}}$ are the basic grid spacings in the x and y directions, respectively. The upper-left indices $i_{ul,m}$ and $j_{ul,m}$ of the cell containing the marker and weights $w_{UL,m}$, $w_{LL,m}$, $w_{UR,m}$, and $w_{LR,m}$ are pre-computed for each marker using bisection to improve the efficiency of the interpolation process. These pre-computed weights and indices can also be used to optimize (C.1) as described in the following algorithm:

1. Calculate the numerator, denoted with subscript n, and denominator, denoted with subscript d, summations from (C.1) by evaluating weights associated with each marker m:

For Each Marker m Do:

$$
\begin{aligned}
S_{avg,d(i_{ul,m},j_{ul,m})} &= S_{avg,d(i_{ul,m},j_{ul,m})} + w_{UL,m} \\
S_{avg,n(i_{ul,m},j_{ul,m})} &= S_{avg,n(i_{ul,m},j_{ul,m})} + S_m w_{UL,m} \\
S_{avg,d(i_{ul,m},j_{ul,m}+1)} &= S_{avg,d(i_{ul,m},j_{ul,m}+1)} + w_{UR,m} \\
S_{avg,n(i_{ul,m},j_{ul,m}+1)} &= S_{avg,n(i_{ul,m},j_{ul,m}+1)} + S_m w_{UR,m} \\
S_{avg,d(i_{ul,m}+1,j_{ul,m})} &= S_{avg,d(i_{ul,m}+1,j_{ul,m})} + w_{LL,m} \\
S_{avg,n(i_{ul,m}+1,j_{ul,m})} &= S_{avg,n(i_{ul,m}+1,j_{ul,m})} + S_m w_{LL,m} \\
S_{avg,d(i_{ul,m}+1,j_{ul,m}+1)} &= S_{avg,d(i_{ul,m}+1,j_{ul,m}+1)} + w_{LR,m} \\
S_{avg,n(i_{ul,m}+1,j_{ul,m}+1)} &= S_{avg,n(i_{ul,m}+1,j_{ul,m}+1)} + S_m w_{LR,m}
\end{aligned}
\tag{C.5}
$$

End marker Loop

2. Calculate bilinear average values at each grid node (i, j) using the numerator and denominator summations:

$$S_{i,j} = \frac{S_{avg,n}(i,j)}{S_{avg,d}(i,j)} \tag{C.6}$$

Appendix D. Non-Linear Creep Viscosity Update Steps

For each marker m do:

1. Initialize the deviatoric stress invariant $\sigma'_{II,A,m}$ using equation (11) with current marker deviatoric shear stress $\sigma'_{xy,m}$ and deviatoric normal stress $\sigma'_{xx,m}$.

2. Calculate effective creep viscosity $\eta_{creep,m}$ using equation (83) with deviatoric stress invariant $\sigma'_{II,A,m}$ and $\dot{\epsilon}_{eff}$ calculated with current marker temperature T_m, pressure P_m and deviatoric stress invariant $\sigma'_{II,A,m}$.

3. Forecast the deviatoric stress invariant $\sigma'_{II,B,m}$ using equation (87) with current creep viscosity $\eta_{creep,m}$.

   While $N_{iterations} < N_{max}$ and $\Delta\sigma > 1$ do:

   (1) Calculate average stress invariant $\sigma'_{II,avg,m}$ using the following equation:

   $$\sigma'_{II,avg,m} = \frac{1}{2}\left(\sigma'_{II,A,m} + \sigma'_{II,B,m}\right) \tag{D.1}$$

   (2) Calculate effective creep viscosity $\eta_{creep,m}$ using equation (83) with deviatoric stress invariant $\sigma'_{II,avg,m}$ and $\dot{\epsilon}_{eff}$ calculated with marker temperature T_m, pressure P_m and deviatoric stress invariant $\sigma'_{II,avg,m}$.

   (3) Update the forecasted visco-elastic stress invariant $\sigma'_{II,fc,m}$ using equation (87) with $\eta_{creep,m}$ and current marker deviatoric shear stress $\sigma'_{xy,m}$ and deviatoric normal stress $\sigma'_{xx,m}$.

(4) Update bisection limits:

if $(\sigma'_{II,B,m} > \sigma_{II,m,A})$ **and** $(\sigma'_{II,fc,m} > \sigma'_{II,avg,m})$ **or** $(\sigma'_{II,B,m} < \sigma'_{II,A,m})$ **and** $(\sigma'_{II,fc,m} < \sigma'_{II,avg,m})$ **then**

$\sigma'_{II,A,m} = \sigma'_{II,avg,m}$

else

$\sigma'_{II,B,m} = \sigma'_{II,avg,m}$

end if

(5) Update the stress change $\Delta\sigma$ using the following equation:

$$\Delta\sigma = \sigma'_{II,B,m} - \sigma'_{II,A,m} \tag{D.2}$$

End while loop

4. Copy updated marker creep viscosity $\eta_{creep,m}$ and copy to $\eta_{vp(m)}$ to initialize visco-plastic marker viscosity for time step.

End marker loop

References

[1] L. Geoffroy, Volcanic passive margins, Comptes Rendus Geoscience 337 (16) (2005) 1395–1408. doi:https://doi.org/10.1016/j.crte.2005.10.006.
URL https://www.sciencedirect.com/science/article/pii/S1631071305003251

[2] D. G. Quirk, A. Shakerley, M. J. Howe, A mechanism for construction of volcanic rifted margins during continental breakup, Geology 42 (12) (2014) 1079–1082. arXiv:https://pubs.geoscienceworld.org/gsa/geology/article-pdf/42/12/1079/3545900/1079.pdf, doi:10.1130/G35974.1.
URL https://doi.org/10.1130/G35974.1

[3] D. Paton, J. Pindell, K. McDermott, P. Bellingham, B. Horn, Evolution of seaward-dipping reflectors at the onset of oceanic crust formation at volcanic passive margins: Insights from the south atlantic, Geology 45 (5) (2017) 439–442. arXiv:https://pubs.geoscienceworld.org/gsa/geology/article-pdf/45/5/439/999321/439.pdf, doi:10.1130/G38706.1.
URL https://doi.org/10.1130/G38706.1

[4] C. McDermott, J. S. Collier, L. Lonergan, J. Fruehn, P. Bellingham, Seismic velocity structure of seaward-dipping reflectors on the south american continental margin, Earth and Planetary Science Letters 521 (2019) 14–24. doi:https://doi.org/10.1016/j.epsl.2019.05.049.
URL https://www.sciencedirect.com/science/article/pii/S0012821X19303322

[5] G. D. Karner, C. Johnson, J. Shoffner, M. Lawson, M. Sullivan, J. Sitgreaves, J. McHarge, J. Stewart, P. Figueredo, Tectono-magmatic development of the santos and campos basins, offshore brazil, in: The Supergiant Lower Cretaceous Pre-Salt Petroleum Systems of the Santos Basin, Brazil, Vol. 124 of AAPG Memoir, AAPG, 2021, Ch. 9, pp. 215–256. doi:10.1306/13722321MSB.9.1853.

[6] E. Lundin, G. Karner, C. Johnson, A. Doré, Distribution and timing of lithospheric breakup across the gulf of mexico: The role of seaward-dipping reflectors, spreading propagators, and crustal shear zones, Geosphere 21 (3) (2025) 470–509. arXiv:https://pubs.geoscienceworld.org/gsa/geosphere/article-pdf/21/3/470/7199089/ges02828.1.pdf, doi:10.1130/GES02828.1.
URL https://doi.org/10.1130/GES02828.1

[7] E. A. Kneller, C. A. Johnson, G. D. Karner, J. Einhorn, T. A. Queffelec, Inverse methods for modeling non-rigid plate kinematics: Application to mesozoic plate reconstructions of the central atlantic, Computers & Geosciences 49 (2012) 217–230.

doi:https://doi.org/10.1016/j.cageo.2012.06.019.
URL https://www.sciencedirect.com/science/article/pii/S0098300412002142

[8] J. Pindell, R. Graham, B. Horn, Rapid outer marginal collapse at the rift to drift transition of passive margin evolution, with a gulf of mexico case study, Basin Research 26 (6) (2014) 701–725. arXiv:https://onlinelibrary.wiley.com/doi/pdf/10.1111/bre.12059, doi:https://doi.org/10.1111/bre.12059.
URL https://onlinelibrary.wiley.com/doi/abs/10.1111/bre.12059

[9] J. B. Naliboff, S. J. H. Buiter, G. Péron-Pinvidic, P. T. Osmundsen, J. Tetreault, Complex fault interaction controls continental rifting, Nature Communications 8 (1) (2017) 1179. doi:10.1038/s41467-017-00904-x.
URL https://doi.org/10.1038/s41467-017-00904-x

[10] T. Theunissen, R. S. Huismans, Mantle exhumation at magma-poor rifted margins controlled by frictional shear zones, Nature Communications 13 (1) (2022) 1634.
URL https://doi.org/10.1038/s41467-022-29058-1

[11] M. Andrés-Martínez, M. Pérez-Gussinyé, J. Armitage, J. P. Morgan, Thermomechanical implications of sediment transport for the architecture and evolution of continental rifts and margins, Tectonics 38 (2) (2019) 641–665. arXiv:https://agupubs.onlinelibrary.wiley.com/doi/pdf/10.1029/2018TC005346, doi:10.1029/2018TC005346.
URL https://agupubs.onlinelibrary.wiley.com/doi/abs/10.1029/2018TC005346

[12] T. Theunissen, R. S. Huismans, Long-term coupling and feedback between tectonics and surface processes during non-volcanic rifted margin formation, Journal of Geophysical Research: Solid Earth 124 (11) (2019) 12323–12347. arXiv:https://agupubs.onlinelibrary.wiley.com/doi/pdf/10.1029/2018JB017235, doi:https://doi.org/10.1029/2018JB017235.
URL https://agupubs.onlinelibrary.wiley.com/doi/abs/10.1029/2018JB017235

[13] T. Theunissen, R. S. Huismans, G. Lu, N. Riel, Relative continent - mid-ocean ridge elevation: A reference case for isostasy in geodynamics, Earth-Science Reviews 233 (2022) 104153. doi:10.1016/j.earscirev.2022.104153.
URL https://www.sciencedirect.com/science/article/pii/S0012825222002379

[14] T. V. Gerya, J.-P. Burg, Intrusion of ultramafic magmatic bodies into the continental crust: Numerical simulation, Physics of the Earth and Planetary Interiors 160 (2) (2007) 124–142.

doi:https://doi.org/10.1016/j.pepi.2006.10.004.
URL https://www.sciencedirect.com/science/article/pii/S0031920106003049

[15] T. V. Gerya, Three-dimensional thermomechanical modeling of oceanic spreading initiation and evolution, Physics of the Earth and Planetary Interiors 214 (2013) 35–52. doi:10.1016/j.pepi.2012.10.007.
URL https://www.sciencedirect.com/science/article/pii/S0031920112001835

[16] E. Ros, M. Pérez-Gussinyé, M. Araújo, M. Thoaldo Romeiro, M. Andrés-Martínez, J. P. Morgan, Lower crustal strength controls on melting and serpentinization at magma-poor margins: Potential implications for the south atlantic, Geochemistry, Geophysics, Geosystems 18 (12) (2017) 4538–4557. arXiv:https://agupubs.onlinelibrary.wiley.com/doi/pdf/10.1002/2017GC007212, doi:https://doi.org/10.1002/2017GC007212.
URL https://agupubs.onlinelibrary.wiley.com/doi/abs/10.1002/2017GC007212

[17] L. Mezri, J. García-Pintado, M. Pérez-Gussinyé, Z. Liu, W. Bach, M. Cannat, Tectonic controls on melt production and crustal architecture during magma-poor seafloor spreading, Earth and Planetary Science Letters 628 (2024) 118569. doi:10.1016/j.epsl.2024.118569.
URL https://www.sciencedirect.com/science/article/pii/S0012821X24000037

[18] W. R. Buck, The role of magmatic loads and rift jumps in generating seaward dipping reflectors on volcanic rifted margins, Earth and Planetary Science Letters 466 (2017) 62–69. doi:https://doi.org/10.1016/j.epsl.2017.02.041.
URL https://www.sciencedirect.com/science/article/pii/S0012821X17301176

[19] X. Tian, W. R. Buck, Lithospheric thickness of volcanic rifting margins: Constraints from seaward dipping reflectors, Journal of Geophysical Research: Solid Earth 124 (4) (2019) 3254–3270. arXiv:https://agupubs.onlinelibrary.wiley.com/doi/pdf/10.1029/2018JB016733, doi:https://doi.org/10.1029/2018JB016733.
URL https://agupubs.onlinelibrary.wiley.com/doi/abs/10.1029/2018JB016733

[20] E. A. Kneller, Earthbox.jl: A visco-elasto-plastic geodynamic modeling framework in julia with marine and terrestrial sediment transport, melt intrusion and extrusion, frictional-plastic melt damage and lava flow modeling, GitHub repository (2025).
URL https://github.com/eakneller/EarthBox.jl

[21] T. Gerya, Introduction to Numerical Geodynamic Modelling, Cambridge University Press, 2010.
URL https://books.google.com/books?id=W83gxp165SkC

[22] T. Gerya, Introduction to Numerical Geodynamic Modelling, Cambridge University Press, 2019.
URL https://books.google.com/books?id=8XGSDwAAQBAJ

[23] F. H. Harlow, J. E. Welch, Numerical calculation of time-dependent viscous incompressible flow of fluid with free surface, The Physics of Fluids 8 (12) (1965) 2182–2189. doi:10.1063/1.1761178.
URL https://doi.org/10.1063/1.1761178

[24] T. V. Gerya, D. A. Yuen, Characteristics-based marker-in-cell method with conservative finite-differences schemes for modeling geological flows with strongly variable transport properties, Physics of the Earth and Planetary Interiors 140 (4) (2003) 293–318. doi:10.1016/j.pepi.2003.09.006.
URL https://www.sciencedirect.com/science/article/abs/pii/S0031920103001900

[25] T. V. Gerya, D. A. Yuen, Robust characteristics method for modelling multiphase visco-elasto-plastic thermo-mechanical problems, Physics of the Earth and Planetary Interiors 163 (1) (2007) 83–105, computational Challenges in the Earth Sciences. doi:10.1016/j.pepi.2007.04.015.
URL https://www.sciencedirect.com/science/article/pii/S0031920107000969

[26] T. Hantschel, A. I. Kauerauf, Fundamentals of Basin and Petroleum Systems Modeling, eBook Packages Earth and Environmental Science, Earth and Environmental Science (R0), Springer Berlin, Heidelberg, 2009. doi:10.1007/978-3-540-72318-9.
URL https://doi.org/10.1007/978-3-540-72318-9

[27] D. L. Turcotte, G. Schubert, Geodynamics, 3rd Edition, Cambridge University Press, Cambridge, 2014. doi:10.1017/CBO9780511843877.

[28] J. G. Sclater, P. A. F. Christie, Continental stretching: An explanation of the post-mid-cretaceous subsidence of the central north sea basin, Journal of Geophysical Research: Solid Earth 85 (B7) (1980) 3711–3739. arXiv:https://agupubs.onlinelibrary.wiley.com/doi/pdf/10.1029/JB085iB07p03711, doi:10.1029/JB085iB07p03711.
URL https://agupubs.onlinelibrary.wiley.com/doi/abs/10.1029/JB085iB07p03711

[29] R. F. Katz, M. Spiegelman, C. H. Langmuir, A new parameterization of hydrous mantle melting, Geochemistry, Geophysics, Geosystems 4 (9) (2003). arXiv:https://agupubs.onlinelibrary.wiley.com/doi/pdf/10.1029/2002GC000433, doi:10.1029/2002GC000433.

URL https://agupubs.onlinelibrary.wiley.com/doi/abs/10.1029/2002GC000433

[30] J. Maclennan, T. Hulme, S. C. Singh, Thermal models of oceanic crustal accretion: Linking geophysical, geological and petrological observations, Geochemistry, Geophysics, Geosystems 5 (2) (2004). arXiv:https://agupubs.onlinelibrary.wiley.com/doi/pdf/10.1029/2003GC000605, doi:10.1029/2003GC000605.
URL https://agupubs.onlinelibrary.wiley.com/doi/abs/10.1029/2003GC000605

[31] J. A. D. Connolly, M. W. Schmidt, G. Solferino, N. Bagdassarov, Permeability of asthenospheric mantle and melt extraction rates at mid-ocean ridges, Nature 462 (7270) (2009) 209–212.
URL https://doi.org/10.1038/nature08517

[32] L. G. J. Montési, M. D. Behn, L. B. Hebert, J. Lin, J. L. Barry, Controls on melt migration and extraction at the ultraslow southwest indian ridge 10ř16ře, Journal of Geophysical Research: Solid Earth 116 (B10) (2011). arXiv:https://agupubs.onlinelibrary.wiley.com/doi/pdf/10.1029/2011JB008259, doi:https://doi.org/10.1029/2011JB008259.
URL https://agupubs.onlinelibrary.wiley.com/doi/abs/10.1029/2011JB008259

[33] L. B. Hebert, L. G. J. Montési, Melt extraction pathways at segmented oceanic ridges: Application to the east pacific rise at the siqueiros transform, Geophysical Research Letters 38 (11) (2011). arXiv:https://agupubs.onlinelibrary.wiley.com/doi/pdf/10.1029/2011GL047206, doi:https://doi.org/10.1029/2011GL047206.
URL https://agupubs.onlinelibrary.wiley.com/doi/abs/10.1029/2011GL047206

[34] C. E. Lesher, F. J. Spera, Chapter 5 - thermodynamic and transport properties of silicate melts and magma, in: H. Sigurdsson (Ed.), The Encyclopedia of Volcanoes (Second Edition), second edition Edition, Academic Press, Amsterdam, 2015, pp. 113–141. doi:10.1016/B978-0-12-385938-9.00005-5.
URL https://www.sciencedirect.com/science/article/pii/B9780123859389000055

[35] E. Stolper, D. Walker, B. H. Hager, J. F. Hays, Melt segregation from partially molten source regions: The importance of melt density and source region size, Journal of Geophysical Research: Solid Earth 86 (B7) (1981) 6261–6271. arXiv:https://agupubs.onlinelibrary.wiley.com/doi/pdf/10.1029/JB086iB07p06261, doi:10.1029/JB086iB07p06261.
URL https://agupubs.onlinelibrary.wiley.com/doi/abs/10.1029/JB086iB07p06261

[36] R. Rongo, V. Lupiano, M. Avolio, D. D'Ambrosio, W. Spataro, G. Trufillo, Cellular automata simulation of lava flows - applications to civil defense and land use planning with a cellular automata based methodology, in: Proceedings of 1st International Conference on Simulation and Modeling Methodologies, Technologies and Applications, SCITEPRESS (Science and Technology Publications, Lda.), 2011, pp. 37–44. doi:10.5220/0003575900370044.

[37] L. J. Connor, C. B. Connor, K. Meliksetian, I. Savov, Probabilistic approach to modeling lava flow inundation: a lava flow hazard assessment for a nuclear facility in armenia, Journal of Applied Volcanology 1 (3) (2012). URL http://www.appliedvolc.com/content/1/1/3

[38] H. R. Dietterich, E. Lev, J. Chen, J. A. Richardson, K. V. Cashman, Benchmarking computational fluid dynamics models of lava flow simulation for hazard assessment, forecasting, and risk management, Journal of Applied Volcanology 6 (1) (2017) 9.
URL https://doi.org/10.1186/s13617-017-0061-x

[39] B. Bos, C. J. Spiers, Frictional-viscous flow of phyllosilicate-bearing fault rock: Microphysical model and implications for crustal strength profiles, Journal of Geophysical Research: Solid Earth 107 (B2) (2002) ECV 1–1–ECV 1–13. arXiv:https://agupubs.onlinelibrary.wiley.com/doi/pdf/10.1029/2001JB000301, doi:10.1029/2001JB000301.
URL https://agupubs.onlinelibrary.wiley.com/doi/abs/10.1029/2001JB000301

[40] G. C. Gleason, J. Tullis, A flow law for dislocation creep of quartz aggregates determined with the molten salt cell, Tectonophysics 247 (1) (1995) 1–23, 30 Years of Tectonophysics a Special Volume in Honour of Gerhard Oertel. doi:https://doi.org/10.1016/0040-1951(95)00011-B.
URL https://www.sciencedirect.com/science/article/pii/004019519500011B

[41] E. Rybacki, M. Gottschalk, R. Wirth, G. Dresen, Influence of water fugacity and activation volume on the flow properties of fine-grained anorthite aggregates, Journal of Geophysical Research: Solid Earth 111 (B3) (2006). arXiv:https://agupubs.onlinelibrary.wiley.com/doi/pdf/10.1029/2005JB003663, doi:https://doi.org/10.1029/2005JB003663.
URL https://agupubs.onlinelibrary.wiley.com/doi/abs/10.1029/2005JB003663

[42] G. Hirth, D. L. Kohlstedt, Rheology of the upper mantle and the mantle wedge: A view from the experimentalists, in: Inside the Subduction Factory, Vol. 138 of Geophysical Monograph Series, American Geophysical Union, Washington, DC, 2003, pp. 83–105. doi:10.1029/138GM06.

[43] I. Katayama, S. ichiro Karato, Low-temperature, high-stress deformation of olivine under water-saturated conditions, Physics

of the Earth and Planetary Interiors 168 (3) (2008) 125–133. doi:https://doi.org/10.1016/j.pepi.2008.05.019.
URL https://www.sciencedirect.com/science/article/pii/S003192010800112X

[44] S. Brune, C. Heine, M. Pérez-Gussinyé, S. V. Sobolev, Rift migration explains continental margin asymmetry and crustal hyper-extension, Nature Communications 5 (1) (2014) 4014.
URL https://doi.org/10.1038/ncomms5014